



# LUND UNIVERSITY

## Effects from Time Dependence of Ice Nucleus Activity for Contrasting Cloud Types

Waman, Deepak; Deshmukh, Akash; Phillips, Vaughan; Jadav, Arti; Patade, Sachin; Jakobsson, Jonas; Bansemmer, Aaron

*Published in:*  
Journal of Atmospheric Sciences

*DOI:*  
[10.1175/JAS-D-22-0187.1](https://doi.org/10.1175/JAS-D-22-0187.1)

2023

*Document Version:*  
Publisher's PDF, also known as Version of record

[Link to publication](#)

*Citation for published version (APA):*  
Waman, D., Deshmukh, A., Phillips, V., Jadav, A., Patade, S., Jakobsson, J., & Bansemmer, A. (2023). Effects from Time Dependence of Ice Nucleus Activity for Contrasting Cloud Types. *Journal of Atmospheric Sciences*, 80, 2013-2039. <https://doi.org/10.1175/JAS-D-22-0187.1>

*Total number of authors:*  
7

### General rights

Unless other specific re-use rights are stated the following general rights apply:  
Copyright and moral rights for the publications made accessible in the public portal are retained by the authors and/or other copyright owners and it is a condition of accessing publications that users recognise and abide by the legal requirements associated with these rights.

- Users may download and print one copy of any publication from the public portal for the purpose of private study or research.
- You may not further distribute the material or use it for any profit-making activity or commercial gain
- You may freely distribute the URL identifying the publication in the public portal

Read more about Creative commons licenses: <https://creativecommons.org/licenses/>

### Take down policy

If you believe that this document breaches copyright please contact us providing details, and we will remove access to the work immediately and investigate your claim.

LUND UNIVERSITY

PO Box 117  
221 00 Lund  
+46 46-222 00 00

## Effects from Time Dependence of Ice Nucleus Activity for Contrasting Cloud Types

DEEPAK WAMAN<sup>Ⓞ</sup>,<sup>a</sup> AKASH DESHMUKH,<sup>a</sup> ARTI JADAV,<sup>a</sup> SACHIN PATADE,<sup>a</sup> MARTANDA GAUTAM,<sup>a</sup>  
VAUGHAN PHILLIPS,<sup>a</sup> AARON BANSEMER,<sup>b</sup> AND JONAS JAKOBSSON<sup>c</sup>

<sup>a</sup> Department of Physical Geography and Ecosystem Science, Lund University, Lund, Sweden

<sup>b</sup> National Center for Atmospheric Research, Boulder, Colorado

<sup>c</sup> Division of Nuclear Physics, Department of Physics, Lund University, Lund, Sweden

(Manuscript received 26 August 2022, in final form 15 March 2023, accepted 21 March 2023)

**ABSTRACT:** The role of time-dependent freezing of ice nucleating particles (INPs) is evaluated with the “Aerosol–Cloud” (AC) model in 1) deep convection observed over Oklahoma during the Midlatitude Continental Convective Cloud Experiment (MC3E), 2) orographic clouds observed over North California during the Atmospheric Radiation Measurement (ARM) Cloud Aerosol Precipitation Experiment (ACAPEX), and 3) supercooled, stratiform clouds over the United Kingdom, observed during the Aerosol Properties, Processes And Influences on the Earth’s climate (APPRAISE) campaign. AC uses the dynamical core of the WRF Model and has hybrid bin–bulk microphysics and a 3D mesoscale domain. AC is validated against coincident aircraft, ground-based, and satellite observations for all three cases. Filtered concentrations of ice (>0.1–0.2 mm) agree with those observed at all sampled levels. AC predicts the INP activity of various types of aerosol particles with an empirical parameterization (EP), which follows a singular approach (no time dependence). Here, the EP is modified to represent time-dependent INP activity by a purely empirical approach, using our published laboratory observations of time-dependent INP activity. In all simulated clouds, the inclusion of time dependence increases the predicted INP activity of mineral dust particles by 0.5–1 order of magnitude. However, there is little impact on the cloud glaciation because the total ice is mostly (80%–90%) from secondary ice production (SIP) at levels warmer than about  $-36^{\circ}\text{C}$ . The Hallett–Mossop process and fragmentation in ice–ice collisions together initiate about 70% of the total ice, whereas fragmentation during both raindrop freezing and sublimation contributes <10%. Overall, total ice concentrations and SIP are unaffected by time-dependent INP activity. In the simulated APPRAISE case, the main causes of persistence of long-lived clouds and precipitation are predicted to be SIP in weak embedded convection and reactivation following recirculation of dust particles in supercooled layer cloud.

**KEYWORDS:** Ice crystals; Ice particles; Secondary ice production; Clouds

### 1. Introduction

Ice particles in natural clouds affect radiative transfer, precipitation, cloud lifetime, and electrification in the atmosphere worldwide (Takahashi 1978; Cantrell and Heymsfield 2005; Lohmann 2006; Kudzotsa et al. 2016; Phillips et al. 2020, hereafter Ph20). Generally, precipitation can be formed by two processes (e.g., Yau and Rogers 1996): 1) the “warm-rain” process in which water droplets collide and coalesce to form warm rain, and 2) the “ice-crystal” process, which involves vapor growth of ice particles forming snow (or “cold” graupel by riming) which may melt to yield “cold rain.” The ice-crystal process may form much of the surface precipitation globally (Field and Heymsfield 2015), even in the midlatitudes and tropics (Lau and Wu 2003).

At temperatures warmer than about  $-36^{\circ}\text{C}$  (Phillips et al. 2007, hereafter Ph07), primary ice is initiated by “heterogeneous ice nucleation” from solid aerosol particles (APs) acting as ice nucleating particles (INPs). A range of solid APs, such as dust, insoluble organics, black carbon (soot), and primary biological aerosol particles (PBAPs), may initiate primary ice by acting as INPs (Hobbs and Locatelli 1969; DeMott 1990; Kanji et al. 2017, hereafter Ka17; Patade et al. 2021).

Two approaches for representing heterogeneous ice nucleation proposed so far are the “singular (time-independent)” hypothesis and the “classical (time-dependent)” nucleation theory. The singular hypothesis is an approximation based on the assumption that ice nucleation is practically an instantaneous process occurring at deterministic temperatures on specific “active” sites (Levine 1950; Langham and Mason 1958; Vali 1994, 2008) characterized by the lowest particle–ice interfacial energy and hence activation of ice takes place when its characteristic temperature is reached (Niedermeier et al. 2011). According to the singular hypothesis, under the same environmental conditions, microscopically identical INPs with the same characteristic temperature nucleate all together. When INPs are exposed to isothermal conditions, this hypothesis neglects all time dependence, and any activation is assumed to happen at the start of the nucleation (Chen et al. 2008). Phillips et al. (2008, hereafter Ph08, their Fig. 1) and Connolly et al. (2009) innovated the concept of the surface density of active sites among

<sup>Ⓞ</sup> Denotes content that is immediately available upon publication as open access.

Supplemental information related to this paper is available at the Journals Online website: <https://doi.org/10.1175/JAS-D-22-0187.s1>.

Corresponding author: Deepak Waman, [deepak.waman@nateko.lu.se](mailto:deepak.waman@nateko.lu.se).

DOI: 10.1175/JAS-D-22-0187.1

© 2023 American Meteorological Society. This published article is licensed under the terms of the default AMS reuse license. For information regarding reuse of this content and general copyright information, consult the AMS Copyright Policy ([www.ametsoc.org/PUBSReuseLicenses](http://www.ametsoc.org/PUBSReuseLicenses)).

Authenticated [deepak.waman@nateko.lu.se](mailto:deepak.waman@nateko.lu.se) | Downloaded 08/15/23 11:34 AM UTC

INPs, enabling the application of the singular hypothesis to any size distribution of an aerosol species in cloud models.

Bigg (1953) proposed that nucleation is a stochastic process with the freezing probability of a given drop depending on its volume and rate of cooling. Carte (1959) and Dufour and Defay (1963) further proposed that in a given interval of time, all drops in a given monodisperse population have the same probability of nucleation, either heterogeneously or homogeneously. Carte (1959) reinterpreted the results of Bigg (1953) by proposing that this probability is proportional to the drop volume. It follows that more immersed aerosol material in a larger drop contains more of the most active INPs, which explains those observations of drop volume being proportional to the freezing probability. However, below the  $-36^{\circ}\text{C}$  level, different drops contain different kinds of APs, and the freezing probability of such drops cannot be the same (Vali and Stansbury 1966). Vonnegut and Baldwin (1984) experimentally observed that heterogeneous ice nucleation is mainly a stochastic process. They studied the freezing of silver iodide and observed that ice formation in supercooled clouds depends not only on the characteristics of the individual silver iodide particles but also on the probability of water molecules coming together in the ice lattice on the solid surface. This may take from several minutes to hours. Since ice nucleation is a probabilistic process, at a given temperature it depends on the surface area of the INP and on the time during which any INP stays in a favorable environment (Chen et al. 2008; Herbert et al. 2014). Modern laboratory observations have confirmed that the ability of INPs to nucleate ice depends on temperature strongly, and on the surface area of the solid material (DeMott 1990; Murray et al. 2012; Ervens and Feingold 2013).

Yet by assessing previous laboratory experiments in the literature, Vali (2014) concluded that the variations in the time scale of exposure to ambient conditions (e.g., changes in the cooling rate) cause only slight perturbations in the temperatures of each INP compared to the range of all freezing temperatures among the INP population. Thus, this implied that time dependence can often be neglected. As ice nucleation is strongly sensitive to temperature, the suggestion was that numerical models can neglect time dependence (Vali 2014) when cooling rates are sufficiently high ( $\sim 1\text{--}2\text{ K min}^{-1}$ ), which corresponds to updraft speeds of about  $1.5\text{--}3\text{ m s}^{-1}$  (Ka17). However, this was not conclusively verified with cloud simulations.

Our recent laboratory experiment by Jakobsson et al. (2022, hereafter Jk22) quantified the time dependence of freezing for immersed INPs from ambient aerosol samples from the real troposphere. They observed an increment in active INP concentrations by 70%–100% (70%–200%) for 2–10 h isothermally. The maximum time dependence was for dust and rural continental samples. These observations were the basis for Jk22 to propose a method for including time dependence in numerical models using various empirical types of parameterizations of INP activity (e.g., the EP).

Such laboratory experiments were argued a decade ago to be consistent with the idea of continuous freezing of supercooled cloud droplets being the largest source of ice in mixed-phase, midlevel stratus clouds especially when there is little entrainment

of APs from the environment (Crosier et al. 2011, hereafter C11; Westbrook and Illingworth 2013, hereafter WI13). C11 and WI13 observed a case of long-lived, thin stratiform clouds over the southern United Kingdom, by vertically pointing radar and aircraft with quasi-steady precipitation for several hours. WI13 argued that since the vertical motions were weak ( $|w| < 1\text{ m s}^{-1}$ ), there was no possibility of significant mixing of environmental INPs into the cloud layer. They further proposed that the cause for this quasi-steady precipitation and the long lifetime of such clouds is that the ice nucleation process is time dependent.

Another possible reason for quasi-steady ice concentrations claimed to have been observed by WI13 is secondary ice production (SIP). Aircraft (Hobbs et al. 1980; Lasher-Trapp et al. 2016, 2021) and modeling (Yano and Phillips 2011; Phillips et al. 2017b; Zhao et al. 2021; Waman et al. 2022, hereafter Wa22) studies of precipitating cold clouds have shown that the observed number concentrations of the total ice particles are typically about three or four orders of magnitude higher than those of available active INPs ( $< 1\text{ L}^{-1}$ ) at temperatures between  $-5^{\circ}$  and  $-25^{\circ}\text{C}$ . Since the lifetime of such deep convective clouds is only about 60–90 min (e.g., Wa22) and SIP is prolific, the time-dependent process of heterogeneous ice nucleation might not be an important process of ice initiation by comparison.

The objective of the present study is to investigate the possible role of the time dependence of INP activity in explaining the observed ice concentrations in long-lived, precipitating cloud systems, while accounting for all the alternative explanations such as SIP. In this study, the time dependence is represented in our Aerosol–Cloud (AC) model following the framework proposed by Jk22 that has been proven to be realistic for real tropospheric aerosols, as noted above. A range of precipitating cloud types (deep convection, orographic and thin midlevel stratiform clouds) observed by aircraft are considered in the present study.

## 2. Field campaigns and observations

The present study focuses on three different campaigns from different locations and periods. These are 1) the Midlatitude Continental Convective Cloud Experiment (MC3E) consisting of deep convective clouds, 2) the Atmospheric Radiation Measurement (ARM) Cloud Aerosol Precipitation Experiment (CAPEX) consisting of orographic clouds, and 3) the Aerosol Properties, Processes And Influences on the Earth's climate (APPRAISE) campaign which observed supercooled long-lived stratiform clouds. These are described as follows.

### a. MC3E

The MC3E campaign was jointly conducted by the National Aeronautics and Space Administration's (NASA) Global Precipitation Measurement program and the U.S. Department of Energy's (DOE) ARM program over north-central Oklahoma, United States, between 22 April and 6 June 2011. The case of a mesoscale convective system (MCS) consisting of deep convective clouds observed during (0900 to 2400 UTC 11 May 2011) MC3E is analyzed here. The aircraft and ground-based measurements and large-scale forcing (LSF) conditions

TABLE 1. Details of optical probes mounted on the sampling aircraft during the field campaigns and corresponding size range considered in the present study.

Campaign	Aircraft	Instruments used to measure cloud properties			
		Ice particles	Size range (mm)	Cloud droplets	Size range ( $\mu\text{m}$ )
MC3E	Citation	2DC	0.2–1.0		
		CIP	0.2–1.5		
		HVPS-v3	0.2–19.2		
ACAPEX	DOE G-1	2DS	0.2–1.28	CDP	2–20
		HVPS	0.2–19.2		
APPRAISE	CFARR U.K. BAe146	2DS-128	0.1–1.28		

of the MC3E campaign are described by Jensen et al. (2016). The case involved a relatively warm cloud base ( $17^{\circ}\text{C}$ ) with cloud tops reaching up to the  $-60^{\circ}\text{C}$  level.

Table 1 provides details about the optical probes mounted on the Citation aircraft (Fig. 1a) which made measurements of hydrometeor properties during the MC3E campaign. The 2D cloud (2DC) and high-volume precipitation spectrometer version 3 (HVPS-v3) probes had shattering corrected tips (Korolev et al. 2011, hereafter K11) while the cloud imaging probe (CIP) had no such tips. The present study included only concentrations of ice particles with maximum dimensions larger than  $200\ \mu\text{m}$  (“NI<sub>200</sub>”) in the validation of ice number concentrations. Moreover, droplet properties such as size, concentrations, and liquid water content (LWC) were measured by the cloud droplet probe (CDP).

Figures 1b–d show the CIP images at various levels in convective cloudy updrafts. From these images, it is evident that the cloud-base regions were dominated by raindrops (about 0.2–1 mm in diameter, Fig. 1b) whereas abundant rimed ice particles and relatively rare pristine ice crystals were observed at about  $-7^{\circ}\text{C}$  level (Fig. 1c). It is also observed that with increasing height, particle size increases and abundant aggregates, and rimed ice particles ( $>1\ \text{mm}$ ) were present aloft (Figs. 1c,d).

Figure 1e shows the observed profiles of dewpoint and air temperature at 0300 UTC 10 May 2011. The convective available potential energy (CAPE) was about  $3500\ \text{J kg}^{-1}$  (Fig. 1e), which is mostly attributed to the moistening of the lower troposphere from large-scale advection (Jensen et al. 2016).

### b. ACAPEX

ACAPEX was conducted by DOE ARM to study aerosol–cloud interactions in atmospheric rivers (ARs) of moisture in the environment during wintertime storms (Leung 2016). The case selected involves orographic clouds that brought significant precipitation due to the landfall of an AR on the U.S. West Coast (Northern California) on 7 February 2015 (1900–2300 UTC).

Table 1 summarizes the aircraft and optical probes used to sample the observed clouds. The DOE G-1 aircraft (Fig. 2a) made passes between the Central Valley and Sierra Nevada and sampled the low-level, postfrontal clouds in coordination with the National Oceanic and Atmospheric Administration’s (NOAA) *Ron Brown* research ship. Both the 2D spectrometer (2DS) and HVPS probes had their tips corrected for

shattering (K11). The approach described above (section 2a, NI<sub>200</sub>) is followed to compare the predicted ice concentrations with the coincident aircraft observations. Several rain gauges were deployed on the ground at stations within the study domain to measure the amount of surface precipitation.

Figures 2b–d show images from the 2DS probe in the ACAPEX at various levels in convective cloudy updrafts. It is observed that the cloud-base regions ( $\sim 7^{\circ}\text{C}$ ) were characterized by raindrops (about 0.2–1 mm in diameter, Fig. 2b). At subzero levels warmer than  $-7^{\circ}\text{C}$ , mostly pristine ice crystals together with rimed ice particles were observed. The average ice particle size is observed to increase from the lower ( $-7^{\circ}\text{C}$ ) to the upper half ( $-18^{\circ}\text{C}$ ) of the mixed-phase region.

The observed APs are typically marine in origin (Fig. 2e). The INPs were mainly marine while dust and soot were scarce (Levin et al. 2019; Lin et al. 2022). The *Ron Brown* ship made observations of atmospheric conditions such as temperature, moisture, winds, aerosols, surface fluxes, and radiative fluxes (Leung 2016). Figure 2f shows observed vertical profiles of air and dewpoint temperatures at 1900 UTC 7 February 2015. The LCL was located at about 953 hPa and the horizontal wind speeds were relatively high ( $\sim 10\ \text{m s}^{-1}$ ) throughout the atmosphere.

### c. APPRAISE

A case of supercooled stratiform clouds with embedded convection was observed over southern England covering an area of about 100 km in width on 18 February 2009 during the APPRAISE campaign. The vertical extent of these clouds was about 4 km and such cloudy conditions persisted in the observed location near Chilbolton for more than a day with continuous precipitation (C11; W113). The U.K. BAe146 Facility for Airborne Atmospheric Measurement (FAAM) aircraft flight track is shown in Fig. 3a which sampled these clouds near the Chilbolton Facility for Atmospheric and Radio Research (CFARR). The cloud base was at about 500 m above mean sea level (MSL) whereas the cloud top was at 4.3 km MSL.

Figure 3c shows observed vertical profiles of air and dewpoint temperatures at 1100 UTC 17 February 2009. The horizontal wind speeds were significantly weak ( $<5\ \text{m s}^{-1}$ ) throughout the atmosphere up to the cloud top ( $\sim -13^{\circ}\text{C}$ ). There was an inversion (a temperature difference of about  $4^{\circ}\text{C}$ ) layer seen above the cloud top characterized by an extremely dry atmosphere aloft with relative humidity (RH) of

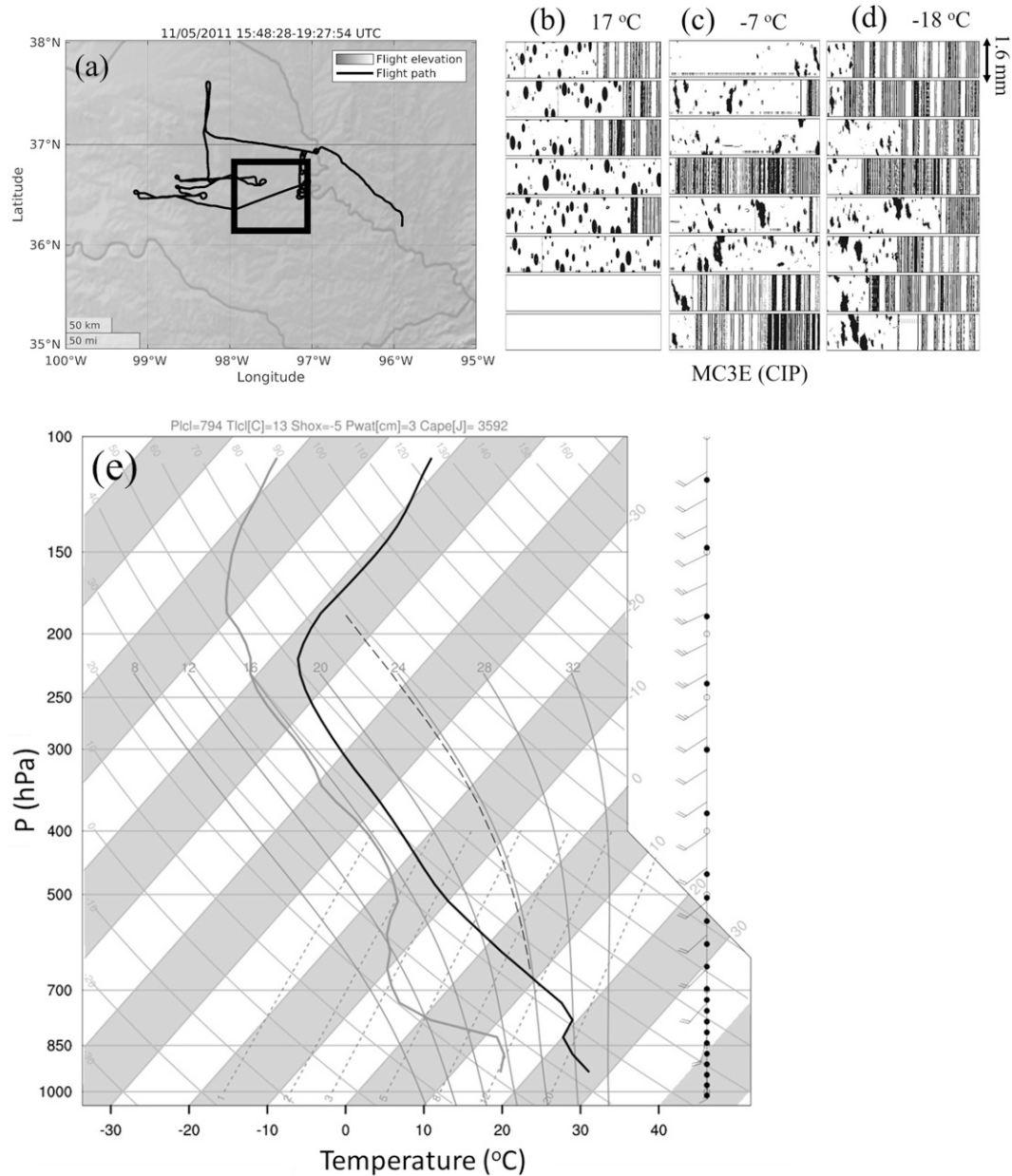


FIG. 1. (a) Profiles of geographical area, flight track of the Citation aircraft (thin black line), and the simulation domain (solid black box), as well as particle images in convective cloudy updrafts ( $w > 1 \text{ m s}^{-1}$ ) shown at (b) 17°C (cloud base), (c) -7°C, and (d) -16°C levels from the CIP mounted on the Citation aircraft during the MC3E campaign on 11 May 2011. (e) Observed vertical profile of the air (solid black line) and dewpoint (solid gray line) temperature and moist adiabat (thin dotted line) for the MC3E case for the same day at 0300 UTC.

less than about 30%. Figure 3c reveals two distinct cloudy layers. A saturated layer ( $\sim 1.5 \text{ km}$  vertical extent) was seen at lower levels between 1000 and 850 hPa. Above the 850 hPa level, the atmosphere was completely dry ( $\text{RH} < 50\%$ ) up to the 700 hPa level. A thin ( $\sim 400 \text{ m}$ ) layer of saturated air was observed above the 700 hPa level, extending up to the cloud top ( $\sim -13^\circ\text{C}$ ). The system was anticyclonic (surface pressure  $\sim 1020 \text{ hPa}$ ) and quasi steady, covering most of the United Kingdom with quasi-steady precipitation for more than a day.

C11 and WI13 highlighted most of the features of the observed system.

Although WI13 claimed that there was a quasi-steady state of the glaciated cloud properties and snowfall, their radar measurements and flights during the campaign did not follow the motions in a Lagrangian sense. WI13 claimed there was minimal cooling in cloud-top temperature (by about 1.5 K) over Chilbolton for a period of more than a day. They further hypothesized that this cooling of the cloud top might have

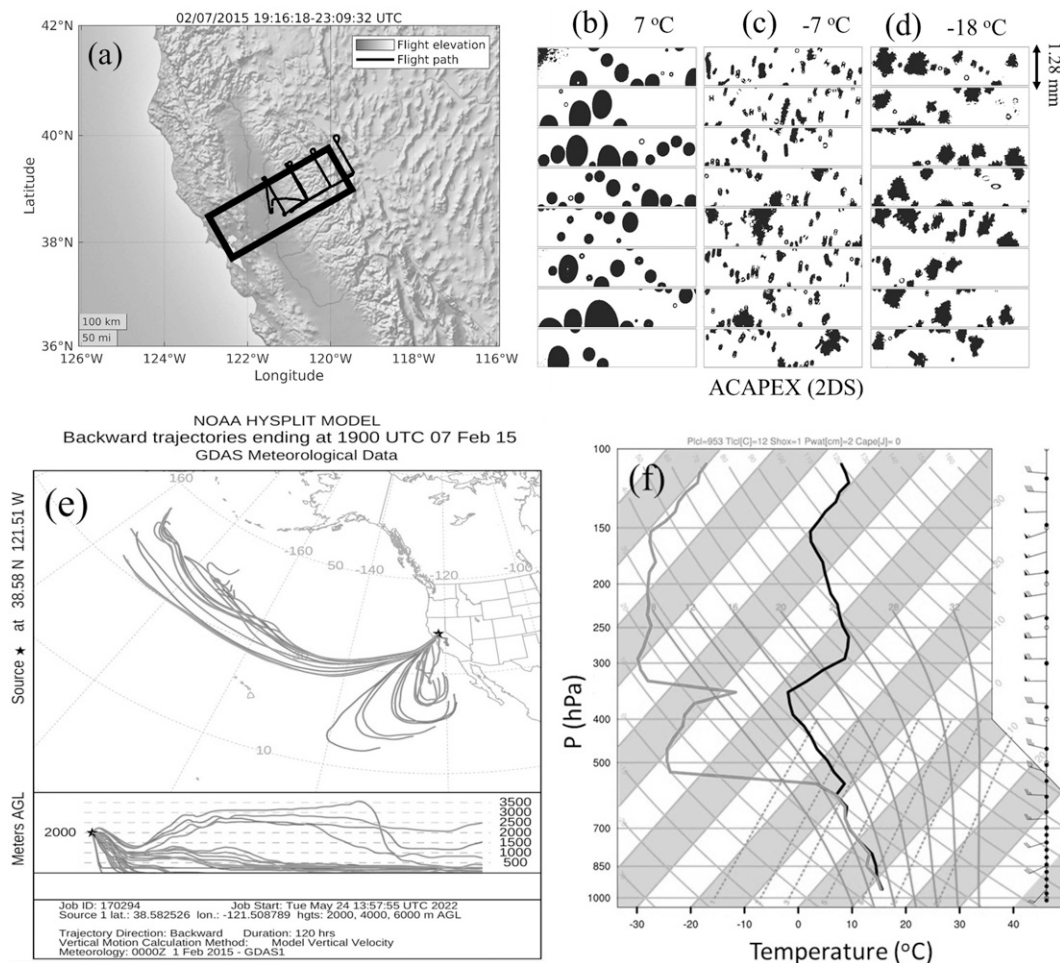


FIG. 2. (a) Profiles of geographical area, flight track of the DOE-G1 aircraft (thin black line), and the simulation domain (solid black rectangle), as well as particle images in convective cloudy updrafts ( $w > 1 \text{ m s}^{-1}$ ) at (b) 7°C (cloud base), (c) -7°C, and (d) -18°C levels from the 2DS probe mounted on the DOE-G1 aircraft during the ACAPEX campaign on 7 Feb 2015. (e) Hybrid Single-Particle Lagrangian Integrated Trajectory (HYSPLIT) backward trajectory for 120 h showing the airflow from the North Pacific Ocean over the study domain (Sacramento, California, United States) on the same day at 1900 UTC. (f) Observed vertical profile of the air (solid black line) and dewpoint (solid gray line) temperature for the same day and time.

increased active INPs. The radar used in [WI13](#) was fixed at one location and pointing vertically. Most of the aerosols were marine in origin as the Hybrid Single-Particle Lagrangian Integrated Trajectory (HYSPLIT) back-trajectory shows the long-range transport over the study domain was mainly from the North Atlantic Ocean ([Fig. 3b](#)) with a mixture of continental APs from France.

In reality, the horizontal wind speed was about  $3 \text{ m s}^{-1}$  southward in the lower troposphere, and this must have advected the sampled clouds by about 300 km in 24 h. This distance is far greater than the span of the aircraft flights and radar sampling. Consequently, it cannot be ruled out that there was substantial time evolution of cloud properties and surface precipitation following the motion. The appearance of a quasi-steady state is explicable in terms of an approximate steady state of the synoptic-scale flow, combined with the time evolution of cloud properties along parcel trajectories.

In fact, [WI13](#) did not actually prove the quasi-steady state of cloud properties following the air motion for more than a day, given the aircraft flights.

Observations from the 2DS probe ([Table 1](#)) were corrected for artificial shattering by applying corrections following [Field et al. \(2006\)](#) and only particles larger than  $100 \mu\text{m}$  (“NI<sub>100</sub>”) were included in the plotted ice concentrations. However, [K11](#) suggests that even after applying these corrections the uncertainty due to the artificial shattering remains. Hence, we further corrected the 2DS data ([WI13](#), their [Fig. 9](#)) by multiplying all measured ice concentrations by a factor of 0.253 inferred from [K11](#) (their [Fig. 5](#), comparison of solid blue and red lines).

### 3. Description of AC model

The present study used AC which was created to represent radiation (Geophysical Fluid Dynamics Laboratory radiation

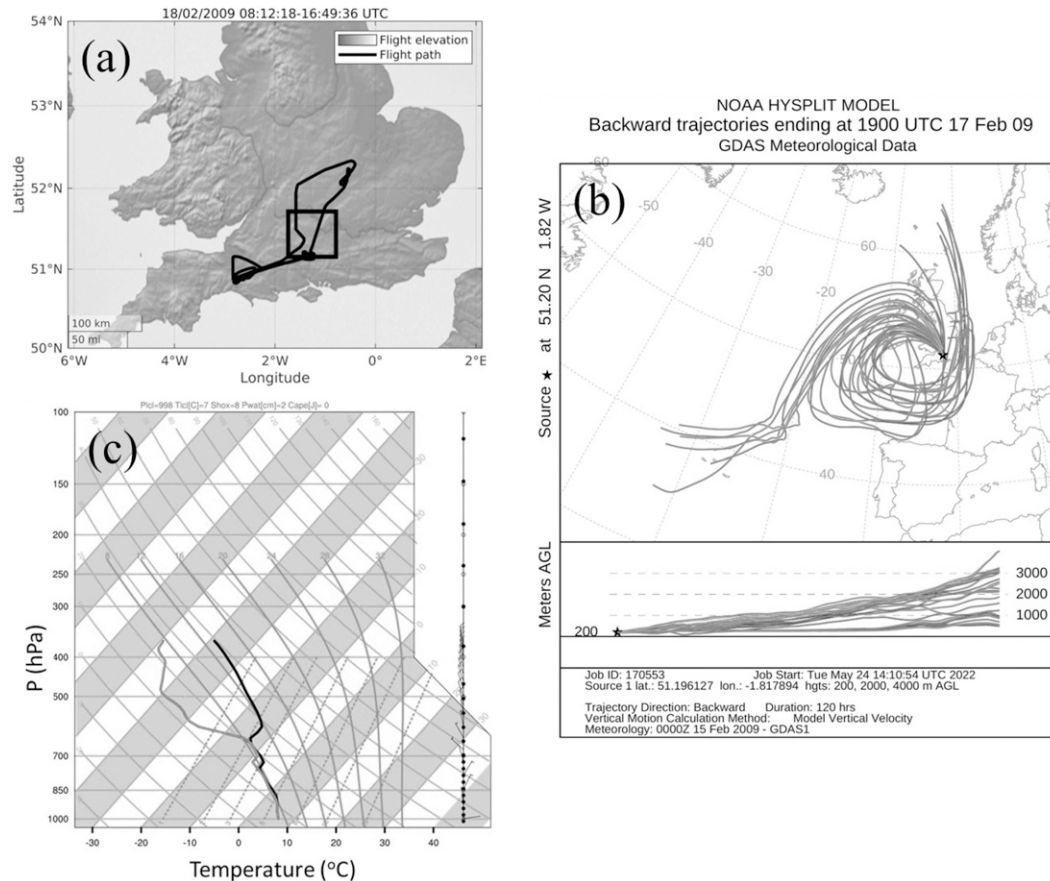


FIG. 3. (a) Profiles of geographical area, flight track of the BAe146 aircraft (thin black line), and the simulation domain (solid black box) during the APPRAISE campaign on 18 Feb 2009. (b) HYSPLIT backward trajectory for 120 h showing the airflow from the North Atlantic Ocean region as well as from the continent (France) over the study domain (Larkhill, United Kingdom) in the APPRAISE case on the same day at 1900 UTC. (c) Observed vertical profile of the air (solid black line) and dewpoint (solid gray line) temperature at 1100 UTC on the same day.

scheme; Freidenreich and Ramaswamy 1999) interactively with cloud properties and has a semiprognostic aerosol scheme. AC treats cloud properties with a hybrid spectral bin–two-moment bulk microphysics scheme (Ph07; Ph08; Phillips et al. 2009, 2013, hereafter Ph13, 2015, 2017a, 2018; Ph20). AC treats the cycling of aerosols through clouds and changes in AP concentrations due to cloud and precipitation by a two-way aerosol–cloud coupling, and tracks components of APs in the air interstitially, immersed in clouds and in precipitation (Phillips et al. 2009).

AC uses the dynamical core of the WRF Model and its software infrastructure (Dudhia 1989; Skamarock et al. 2005). AC treats turbulence using the Medium Range Forecast (MRF) model planetary boundary layer (PBL) scheme which resolves the vertical subgrid-scale fluxes (Hong and Pan 1996) and uses some other standard WRF schemes such as for the surface layer (Monin and Obukhov 1954) and dynamics. AC has been used in previous studies (e.g., Phillips et al. 2017b; Ph20; Patade et al. 2022; Wa22).

AC represents microphysical species as cloud liquid, cloud ice (“crystals”), snow, graupel/hail, and rain. The total number

and mass (“two-moment approach”) mixing ratios of each of these species are diffused and advected as bulk prognostic variables in AC. The components of mass and number concentrations of cloud ice and snow initiated in various processes (heterogeneous and homogeneous freezing, four mechanisms of SIP) are tracked by extra prognostic variables in AC. Soluble APs such as ammonium sulfate, sea salt, and soluble organics (sO) initiate cloud droplets in AC at cloud base (Ming et al. 2006) and at in-cloud levels far above cloud base from the supersaturation resolved on the model grid, (“in-cloud droplet activation”) (Ph07; Phillips et al. 2009).

Insoluble APs such as mineral dust (DM), soot (BC), and five types of PBAPs (Patade et al. 2021, section 3.1 therein) initiate primary ice in AC at levels warmer than  $-36^{\circ}\text{C}$  through heterogeneous ice nucleation. These insoluble APs also initiate cloud droplets as they tend to have hydrophilic coatings or are wettable. AC predicts the INP activity of these insoluble APs with the EP [section 3a(1)] (Ph08; Ph13). The EP represents all modes of INP activation (deposition mode, freezing modes of contact, condensation, and immersion) depending on the temperature, surface area mixing ratio

of each AP type and supersaturation. Both inside-out and outside-in contact freezing is treated.

AC forms ice homogeneously by two mechanisms. First, spontaneous freezing of supercooled cloud drops and raindrops above about  $-36^\circ\text{C}$  level forms ice depending on the drop size. There is preferential evaporation of the smaller cloud droplets in the size distribution that freeze later during ascent through the layer of homogeneous freezing of cloud liquid (about  $-35^\circ$  to  $-37^\circ\text{C}$ ), with a lookup table (Ph07). Second, homogeneous aerosol freezing occurs at colder temperatures as soon as a critical supersaturation is exceeded with respect to ice. This critical supersaturation depends on the temperature and size of APs (Koop et al. 2000; Ph07).

#### a. Time-dependent heterogeneous ice nucleation in AC

##### 1) PREVIOUS REPRESENTATION WITH EP IN AC WITHOUT TIME DEPENDENCE

In AC, for the  $X$ th ( $X = \text{DM, BC, sO, and PBAPs}$ ) species of APs that are or can become solid (section 3a), the EP gives the number mixing ratio ( $n_{\text{IN},X}$ ) of active INPs (Ph08; Ph13) at the ambient temperature ( $T$ ) and humidity (related to  $S_i$ ),

$$n_{\text{IN},X}(T, S_i, \Omega_X) = \int_{\log(0.1\mu\text{m})}^{\infty} \{1 - \exp[-\mu_X(D_X, S_i, T)]\} \times \frac{dn_X}{d \log D_X} \times d \log D_X. \quad (1)$$

For  $X = \text{DM, BC, and sO}$ ,

$$\mu_X = H_X(S_i, T) \xi(T) \left( \frac{\alpha_X n_{\text{IN},1,*}}{\Omega_{X,1,*}} \right) \times \frac{d\Omega_X}{dn_X} \quad \forall T < 0^\circ\text{C} \quad \text{and} \quad 1 < S_i \leq S_i^w. \quad (2)$$

Here,  $\Omega_X$  is the surface area mixing ratio for the  $X$ th AP species, and  $\mu_X$  gives the average number of activated ice embryos per solid AP of size  $D_X$ . The scarcity of heterogeneous ice nucleation in subsaturated conditions is represented by the empirically determined fraction  $H_X$ , which is a function of saturation ratio of water vapor with respect to ice ( $S_i$ ) and  $T$ , varying between 0 and 1. The next term,  $\xi$ , is the temperature-dependent fraction representing freezing of INPs immersed in drops and also varies from 0 to 1 for temperatures between  $-2^\circ$  and  $-5^\circ\text{C}$ ;  $S_i^w$  is the value of  $S_i$  at exact water saturation  $S_w$ . Also,  $d\Omega_X/dn_X \approx \pi D_X^2$ . The term  $n_{\text{IN},1,*}$  is the number of active INPs per kg of air and represents the reference activity spectrum (denoted by \*) of the average concentration of INPs. Symbols used in the present study are listed in the appendix (Table A1). More details can be found in Ph08 and Ph13.

Also, for  $X = \text{FNG, PLN, BCT, and DTS}$ ,

$$\mu_X = H_X(S_i, T) \xi(T) \times \text{MIN}\{[\exp(-\gamma_X T) - 1], 40\} \times \frac{1}{\omega_{X,1,*}} \times \frac{d\Omega_X}{dn_X} \quad \forall T < 0^\circ\text{C}. \quad (3)$$

Here,  $\omega_{X,1,*}$  is the baseline coefficient of the group of  $X$ th species in the PBAP group. A different approach is followed to

predict the INP activity from algae. More details can be found in Patade et al. (2021).

The number of ice crystals initiated ( $\Delta n_i$ ) in a time step ( $\Delta t$ ) is incremented by

$$\Delta n_i = \sum_X \text{MAX}(n_{\text{IN},X} - n_{X,a}, 0) \equiv \sum_X \Delta n_{X,a}. \quad (4)$$

Here,  $n_{X,a}$  is the number mixing ratio of INPs from group  $X$  that has already been activated.

Insoluble APs are internally mixed with various types of soluble material (Clarke et al. 2004). When the  $s_w$  reaches a critical value, they form cloud droplets, and the insoluble part becomes immersed in the droplet. A raindrop containing immersed INPs may nucleate ice heterogeneously at subzero temperatures. The number concentrations of INPs activated during heterogeneous raindrop freezing (Ph08) during a time step ( $\Delta t$ ) is

$$d[\Delta n_{\text{IN},\text{rain}}(T, S_i, \Omega_X)] \approx \Delta t \text{MIN}\left[ (w - v_t) \frac{\partial T}{\partial z}, 0 \right] \times \frac{d}{dT} \{n_{\text{IN},1,*}[T, S_i^w(T)]\} \times \sum_X \left( \frac{\alpha_X d\Omega_{X,\text{rain}}}{\Omega_{X,1,*}} \right). \quad (5)$$

Here,  $w$  is the vertical velocity,  $v_t$  is the fall speed of raindrops, and  $d\Omega_{X,\text{rain}} = \Omega_{X,\text{rain}} dQ_r/Q_r$  denotes the surface area mixing ratio of INPs immersed in raindrops. Also,  $Q_r$  is the mass mixing ratio of rain. More details can be found in Ph08.

In summary, Eqs. (1)–(5) represent heterogeneous ice nucleation with the singular approximation.

##### 2) MODIFICATION OF EP TO INCLUDE TIME DEPENDENCE OF INP ACTIVITY

Jk22 proposed an empirical approach relying on a temperature shift [ $\Delta T_X = \Delta T_X(t^*) \leq 0$ ] to represent the time-dependent freezing of active INPs. This was based on their laboratory observations during isothermal experiments over many hours with drop populations (section 1). The temperature input to the EP [section 3a(1)] representing heterogeneous ice nucleation [Eqs. (1) and (7)] is modified by adding the temperature shift for each AP type to represent the observed time-dependent activation. More details are given by Jk22 (their section 3.2.2).

According to Jk22, the temperature shift is

$$\Delta T_X(t^*) = -A_X t^{*\beta}; \quad (6)$$

$t^*$  is the time since the parcel entered the glaciating part of a cloud (the age of the cold parcel). Here,  $t^*$  is estimated by a passive tracer ( $Q$ ) that decays exponentially with time following the motion of any parcel in a cold cloud [ $T < 0^\circ\text{C}$  and ice water content (IWC)  $> 10^{-6} \text{ kg m}^{-3}$ ]. The evolution of  $Q$  is from numerical integration during the simulation of

$$\frac{DQ}{dt} = \begin{cases} \frac{-Q}{\tau_Q} & \forall T < 0^\circ\text{C} \quad \text{and} \quad \text{IWC} > 10^{-6} \text{ kg m}^{-3} \\ 0 & \text{otherwise} \end{cases}. \quad (7)$$

Here,  $\tau_Q$  is an arbitrary relaxation time and is set to 1800 s throughout the simulation. For an adiabatic parcel, the analytical solution of Eq. (6) gives  $t^*$ ,

$$t^* \approx -\tau_Q \ln(Q/Q_0). \quad (8)$$

Outside of the cold cloud,  $Q = Q_0 = 1 \text{ kg}^{-1}$  is prescribed everywhere. Effects on  $t^*$  from dilution of actual simulated parcels are approximately represented by virtue of in-cloud mixing and entrainment being treated in the numerical prediction of  $Q$ .

With this temperature shift  $[\Delta T_X(t^*)]$ , the time-dependent number mixing ratio of active INPs ( $\tilde{n}_{\text{IN},X}$ ) in the  $X$ th species from Eq. (1) is

$$\tilde{n}_{\text{IN},X}(T, S_i, \Omega_X, t) = n_{\text{IN},X} \{ [T + \Delta T_X(t^*)], S_i [T + \Delta T_X(t^*)], \Omega_X \}. \quad (9)$$

Similarly, the time-dependent number mixing ratio of INPs activated in heterogeneous raindrop freezing  $[d(\Delta \tilde{n}_{\text{IN},\text{rain}})]$  from Eq. (5) is obtained by summing over each raindrop size bin,

$$d[\Delta \tilde{n}_{\text{IN},\text{rain}}(T, S_i, \Omega_X)] = d(\Delta n_{\text{IN},\text{rain}} \{ T + \Delta T_X(t^*), S_i [T + \Delta T_X(t^*)], \Omega_X \}). \quad (10)$$

### b. SIP mechanisms represented in AC

AC initiates secondary ice by four types of SIP mechanisms involving fragmentation. These four types are briefly described below.

#### 1) THE HALLETT–MOSSOP PROCESS

The Hallett–Mossop (HM) process involves the emission of small ice splinters during the riming of supercooled cloud droplets between  $-3^\circ$  and  $-8^\circ\text{C}$  (Hallett and Mossop 1974). The maximum splinter emission rate was observed at  $-5^\circ\text{C}$  level and was 350 splinters per milligram of rime particle. This process mainly requires a warm base because another condition is that the cloud droplets emitting splinters must be larger than  $24 \mu\text{m}$  in diameter (Mossop 1976). In AC, this dependence is treated with a cloud-droplet size-dependent factor, which is zero and unity for a mean droplet diameter less than  $16 \mu\text{m}$  and greater than  $24 \mu\text{m}$ , respectively. This factor is linearly interpolated in between. The factor multiplies the emission rate, together with another factor to represent the temperature dependence.

#### 2) FRAGMENTATION IN ICE–ICE COLLISIONS

The second mechanism by which AC forms secondary ice is fragmentation in ice–ice collisions (Phillips et al. 2017a,b). The formulation uses the principle of energy conservation to treat all types of ice particle collisions. A small fraction of the initial collision kinetic energy (CKE) is converted to create the ice fragments. These collisions depend on the size of the colliding ice particles, CKE, and temperature.

The formulation was modified considering a recent field campaign during winter in northern Sweden (Vindeln;  $64.20^\circ\text{N}$ ,  $19.71^\circ\text{E}$ ) to observe the fragmentation of natural snowflakes impacting an array of fixed ice spheres (Martanda 2022). The rime fraction was seen to be better treated by a uniform value at all sizes larger than 2 mm diameter and being linearly interpolated to zero at 0.2 mm.

#### 3) RAINDROP FREEZING FRAGMENTATION

The empirical formulation by Phillips et al. (2018) which initiates secondary ice during the freezing of drizzle/raindrops by two modes is used in AC. In the first mode, there is quasi-spherical freezing when a supercooled drop (0.05–5 mm diameter) collides with a less massive ice particle or during heterogeneous raindrop freezing due to immersed INPs. Secondary splinters form when the outer ice shell breaks during freezing. In the second mode, collisions between a raindrop and a more massive ice particle result in the emission of secondary drops from a splash. Some of these contain ice such that they freeze (Phillips et al. 2018; James et al. 2021).

#### 4) SUBLIMATION BREAKUP OF DENDRITIC SNOW AND GRAUPEL

Secondary ice has been observed to form during the sublimation of dendritic snow and graupel (Oraltay and Hallett 1989; Dong et al. 1994; Bacon et al. 1998). This is represented by the empirical formulation from Deshmukh et al. (2022) in AC. If present, sublimational breakup can be a prolific SIP mechanism in deep convective descent with a quasi equilibrium between emission and total sublimation of fragments (Deshmukh et al. 2022; Wa22).

### c. Experimental setup

All three cases (section 2) have been simulated by AC for a 3D mesoscale domain for the horizontal and vertical resolution of about 2 and 0.5 km, respectively, with an integration time step of 10 s. A modeling study by Pauluis and Garner (2006) revealed that this 2 km horizontal resolution adequately represents the statistics of cloud properties and vertical velocity in deep convective clouds. Little sensitivity to alteration of this resolution was found.

The experimental design is as follows.

#### 1) MC3E

The MC3E case (section 2a) is simulated with a domain of  $80 \text{ km} \times 80 \text{ km}$ . The LSF tendencies of potential temperature ( $\theta$ ) and vapor mixing ratio ( $q_v$ ) were applied (Xie et al. 2014; Jensen et al. 2016). These tendencies were updated hourly and continuously interpolated over time between updates. Lateral boundary conditions (LBC) are periodic in both north–south and east–west directions. Convection is simulated in an idealized way, in the sense that no attempt is made to predict the exact locations of the cloud. Convection was initialized by adding random perturbations (of up to  $\pm 0.06 \text{ g kg}^{-1}$ ) to the initial vapor mixing ratio in the PBL.

AC resolves nonbiological insoluble organics and five types of PBAPs as separate species including fungi (FNG), bacteria

TABLE 2. Aerosol mass mixing ratios near the ground, inferred from observations or from a global model, for various AP species of AC for the case of MC3E (averaged for 9 and 12 May 2011), ACAPEX, both from the IMPROVE measurements, and APPRAISE from the MERRA-2-GIOVANNI model monthly (February 2009) mean values. PBAP measurements from Amazonia (Patade et al. 2021) are used to partition the total PBAP mass (assumed to be 50% of the coincident insoluble organic mass) among the five PBAP groups according to the same ratio. None of these groups was either observed or available from global models.

Aerosol species	Mass concentrations ( $\mu\text{g m}^{-3}$ )		
	MC3E	ACAPEX	APPRAISE
Ammonium sulfate	0.7	0.18	1.8
Sea salt	0.06	0.02	8.0
Mineral dust	0.17	0.030	8.7
soot	0.25	0.015	4.6
Soluble organic	1.36	0.28	1.24
Nonbiological insoluble organics (50% of insoluble organics)	0.17	0.011	0.14
PBAP (50% of insoluble organics)			
Fungi	0.17	0.0042	0.14
Bacteria	0.067	0.0014	0.055
Pollen	0.022	0.0018	0.018
Detritus	0.054	0.0033	0.024
Algae	$4.3 \times 10^{-5}$	$2.7 \times 10^{-6}$	$3.58 \times 10^{-5}$

(BCT), pollen (PLN), detritus (DTS), and algae (ALG) (Patade et al. 2021, section 3.2 therein). It is parsimoniously assumed that about 50% of the measured loading of total insoluble organics consists of PBAPs in the absence of coincident observations of this fraction. Since the loadings of these five types were not measured in the MC3E, their ratio is assumed to follow measurements from Amazonia (Patade et al. 2021).

The Goddard Chemistry Aerosol Radiation and Transport (GOCART) model is used to prescribe the initial mass concentrations of various APs such as ammonium sulfate, sea salt, mineral dust, soot, soluble and insoluble organics for the same month and location. The vertical profiles of each AP are then rescaled by a constant factor to match with observations from the Interagency Monitoring of Protected Visual Environments (IMPROVE) located near the simulated domain. Table 2 summarizes the aerosol mass mixing ratio for each species observed at the ground.

## 2) ACAPEX

The case of orographic stratiform clouds observed during the ACAPEX campaign (section 2b) has been simulated for a horizontal area of  $360 \text{ km} \times 80 \text{ km}$ . The simulation was performed for 3 h (1915–2215 UTC 7 February 2015) and hourly thermodynamic soundings from the *Ron Brown* ship were applied. There were weak cells of embedded convection observed and these were represented by initializing the simulation with eight cold (about  $-5^\circ\text{C}$ ) dry bubbles oriented in a line parallel to the east and west boundaries. These cold

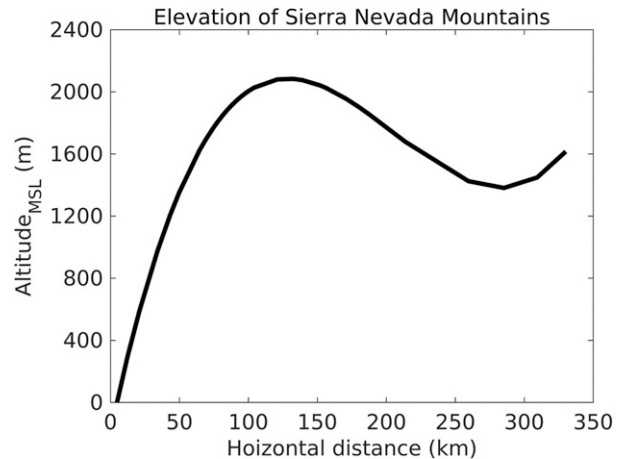


FIG. 4. Schematic picture of ground elevation represented in AC for the simulated ACAPEX case.

bubbles were each separated horizontally by 10 km and superimposed with many small warmer bubbles. Each cold bubble had maximum temperature perturbations of about  $-3 \text{ K}$ . The same approach described in section 3c(1) is followed to obtain the initial mass concentrations of APs (Table 2). LBCs are open and periodic in the  $x$  and  $y$  directions, respectively.

Most of the length of the domain spanned the westernmost mountains in the Sierra Nevada range. The  $x$  and  $y$  axes were rotated by about  $30^\circ$  anticlockwise to orient the long edges of the domain to be perpendicular to the mountain chain (Fig. 2a). The western end of the domain was the Pacific coast. The elevation of the ground is represented in an idealized way as a function only of horizontal distance from the coast (Fig. 4).

## 3) APPRAISE

The case of supercooled, long-lived stratiform clouds observed during the APPRAISE campaign has been simulated for an area of  $80 \text{ km} \times 80 \text{ km}$ . Random perturbations of about  $\pm 0.8 \text{ g kg}^{-1}$  were added to the initial vapor mixing ratio in the PBL to initialize convection. The simulation time is 48 h (0000 UTC 17 February–0000 UTC 19 February 2009), with the first 24 h as a spinup time of the model. LBCs are periodic in both the  $x$  and  $y$  directions.

Hourly fifth-generation European Centre for Medium-Range Weather Forecasts (ECMWF) atmospheric reanalysis (ERA5) data are used to derive the temperature, pressure, RH, and zonal ( $u$ ) and meridional ( $v$ ) wind in the  $x$  and  $y$  directions. The LSF advective tendencies in  $\theta$  and  $q_v$  were applied to the simulation in view of the doubly periodic boundary conditions. These tendencies were estimated from the ERA5 dataset for every hour using

$$\left(\frac{\partial \theta}{\partial t}\right)_{\text{LS}} = \left[ -\left(u \frac{\partial T}{\partial x} + v \frac{\partial T}{\partial y}\right) - \omega \left(\frac{\partial T}{\partial p} - \frac{\alpha}{C_p}\right) \right] \times \left(\frac{p}{p_{1000\text{hPa}}}\right)^{-0.286}, \quad (11)$$

$$\left(\frac{\partial q_v}{\partial t}\right)_{\text{LS}} = -\left(u \frac{\partial q_v}{\partial x} + v \frac{\partial q_v}{\partial y}\right) - \omega \left(\frac{\partial q_v}{\partial p}\right), \quad (12)$$

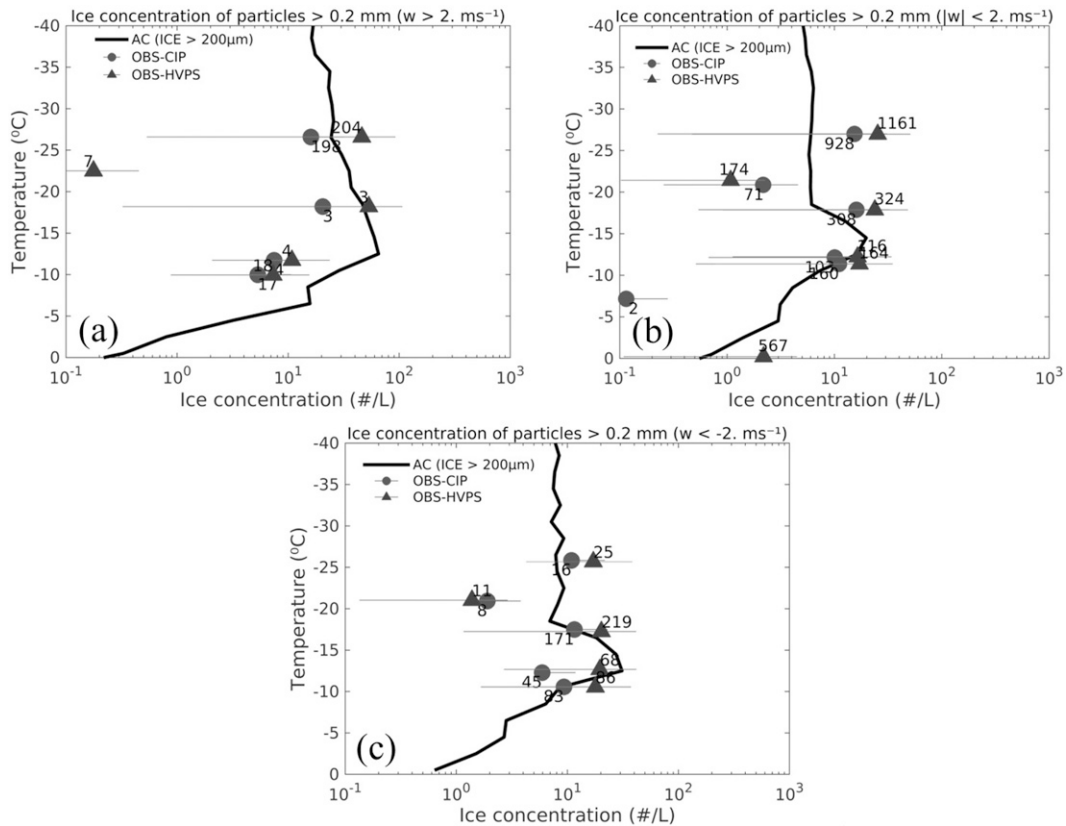


FIG. 5. Comparison of predicted ice number concentrations for particles of maximum dimension bigger than  $200 \mu\text{m}$  ( $\text{NI}_{200}$ ) of all microphysical species (cloud ice, snow, and graupel/hail) from the control simulation of the simulated MC3E case (full black lines) with coincident aircraft observations from the CIP (circles) and HVPS-v3 (upward-pointing triangles) probes over cloudy convective (a) updrafts ( $w > 2 \text{ m s}^{-1}$ ), (b) downdrafts ( $w < -2 \text{ m s}^{-1}$ ), and (c) stratiform ( $|w| < 2 \text{ m s}^{-1}$ ) regions. Numbers by observational data points indicate the total number of seconds for which the aircraft sampled the cloud.

where  $\omega$  is the vertical velocity in pressure coordinates,  $\alpha$  is the specific volume, and  $C_p$  is the specific heat capacity of air at constant pressure. The values of  $\theta$  and  $q_v$  are nudged toward observations for every hour in the lowest 2 km.

The GOCART model is used to prescribe the initial mass concentrations of various APs (Table 2). The vertical profiles of each AP are then rescaled by a constant factor to match with that from the Modern-Era Retrospective Analysis for Research and Applications version 2 (MERRA-2), 2D monthly mean data at the surface ( $\sim 300 \text{ m MSL}$ ). Corrections were applied to MERRA-2-derived mass concentrations of soot and soluble organics to match the predicted cloud condensation nuclei (CCN) activity spectrum with previous maritime observations (e.g., Hoppel et al. 1990).

Furthermore, the initial 24 h are omitted from both the MC3E and APPRAISE simulations. This is because layer clouds advected into the study domain (in MC3E case; Jensen et al. 2015) and slowly evolving ( $|w| < 1 \text{ m s}^{-1}$ ) stratiform clouds (in APPRAISE case) cannot be well measured by sounding arrays that may potentially bias the LSF tendencies.

#### 4. Results from the control simulations from all three cases

##### a. Model validation

##### 1) MC3E

Figure 5 shows a comparison of the predicted filtered ice concentration,  $\text{NI}_{200}$  from the control simulation (Table 3)

TABLE 3. List of simulations performed with AC.

Run performed	Description
Control	Including all four SIP processes and time-dependent heterogeneous freezing
No time-dependent INP	Including all four SIP mechanisms and excluding time dependence of heterogeneous freezing
No dust from droplet evaporation	Excluding contribution to mineral dust in the air from droplet evaporation from the control simulation

with the coincident aircraft observations. In cloudy convective regions (updrafts and downdrafts) and stratiform regions, the predicted  $NI_{200}$  is on the order of about  $10 L^{-1}$  at most observational levels, the same order of magnitude as in the aircraft data (Figs. 5a–c). Furthermore, in the dendritic regions of the stratiform (Fig. 5b) and downdraft (Fig. 5c) regions, the model agrees well with the observed  $NI_{200}$ , differing by less than  $\pm 15\%$  from the aircraft observations at these levels.

Also, predictions of active CCN and INP concentrations, cloud-droplet properties, rainfall rate, radar reflectivity, top of the atmosphere radiative fluxes, and ascent statistics by AC of this MC3E case have already been validated with coincident aircraft, ground-based instruments, and satellite observations in Wa22.

## 2) ACAPEX

Figure 6 shows a comparison of the control simulation with the coincident aircraft and ground-based observations for the simulated ACAPEX case. All predicted microphysical properties (Figs. 6a–e) were averaged conditionally over cloudy convective updrafts ( $w > 1 \text{ m s}^{-1}$ ). Properties of cloud droplets such as mean diameter (Fig. 6a), and LWC (Fig. 6b) are in good agreement with observations from the CDP with errors of less than about 40%.

The predicted value of  $NI_{200}$  in cloudy convective updrafts has the same order of magnitude (about  $10 L^{-1}$ ) as observed by the 2DS probe. The predicted distribution of updraft speeds (Fig. 6d) and the domain-averaged surface precipitation rate at Lake Tahoe (Fig. 6e) each differ by less than 30% from the aircraft observations. Also, the difference between predicted microphysical properties (Figs. 6a–c) and aircraft observations at any level is less than that between the adjacent observational data points, signifying that the model agrees adequately with the observations.

## 3) APPRAISE

For the control simulation of the APPRAISE case, predicted microphysical properties such as  $NI_{100}$  and cloud droplets are compared with the aircraft (BAe146) observations from WI13.

Figure 7a shows adequate agreement of predicted CCN with previous studies such as Twomey and Wojciechowski (1969), Hoppel et al. (1990), and Jennings et al. (1998), in view of the spread of these observations. The number concentrations of cloud droplets (Fig. 7b), LWC (Fig. 7c), and  $NI_{100}$  (Fig. 7d) are all validated adequately with the coincident aircraft observations. The observed ice concentrations have been corrected for the shattering bias as noted above (section 2c). No in situ measurements were reported at levels below 3.6 km as the BAe146 aircraft mainly carried out measurements near cloud-top regions.

A distinct feature of the APPRAISE clouds is that they consisted of episodes of 1) weak embedded convection ( $\sim 0000$ – $1200$  UTC) (“weak embedded convection episode”), and 2) supercooled, long-lived layer clouds ( $\sim 1200$ – $2400$  UTC) (“long-lived layer-cloud episode”), as evident from the observed radar reflectivity (Figs. 7e,f). Our simulation predicts these clouds

adequately (Figs. 7g,h). Figure 7e shows adequate agreement of predicted radar reflectivity for the episodes of weak embedded convection with observations from the 3 GHz Doppler-polarization radar (1219–1221 UTC; C11). In these weak convective cells, the observed and predicted reflectivity values are between 7 and 30 dBZ. A time–height profile of the simulated radar reflectivity (Fig. 7f) is compared with the 35 GHz vertically pointing radar (adopted from C11) located at Chilbolton (Fig. 7i). At 1200 UTC 18 February 2009, the observed reflectivity is between  $-10$  and 3 dBZ for altitudes between 2.5 and 3.8 km, over Chilbolton. The domainwide average of the predicted reflectivity at this time and altitude mostly varies between about  $-10$  and 5 dBZ (Fig. 7g). Both observed (Figs. 7e,f) and predicted cloud tops were at about 4 km (Fig. 7g).

## b. Other analyses of control simulations

### 1) CLOUD-MICROPHYSICAL QUANTITIES

Figures 8a and 8b show the vertical profiles of water contents of various microphysical species for the simulated MC3E, and ACAPEX cases in the stratiform regions ( $|w| < 1 \text{ m s}^{-1}$ ). A distinct feature of the simulated MC3E and ACAPEX cases is that the “ice-crystal process” is the dominant process of precipitation formation at all subzero levels. In both MC3E and ACAPEX cases (Figs. 10a,b), liquid water is predicted to dominate the cloud condensate at levels between the cloud base and  $-5^\circ\text{C}$ , yet at levels between  $-5^\circ\text{C}$  and cloud top is dominated mostly by snow, graupel, and cloud ice (Figs. 8a,b; also Figs. 2, 3 in the online supplement). The presence of abundant snow, graupel, and cloud-ice mass along with strong vertical velocities ( $w > 1 \text{ m s}^{-1}$ , Fig. 8c) and relatively strong wind shear (Fig. 8d) is predicted to enhance SIP through various mechanisms (section 3b). Similar results are predicted in the updraft and downdraft regions (not shown here).

By contrast, in the APPRAISE clouds, the ice-crystal process is predicted to be less active. This can be mainly attributed to relatively less liquid and ice hydrometeors mass (Fig. 8c) and weak vertical velocities ( $|w| \sim 1 \text{ m s}^{-1}$ , Fig. 8d). However, C11 observed that in the episodes of weak embedded convection ( $\sim 0000$ – $1200$  UTC, Fig. 7g), SIP (through the HM process) was mainly active. On the other hand, WI13 observed that in the episodes of long-lived supercooled layer clouds, heterogeneous ice nucleation is the most prolific ice initiation mechanism (Figs. 7e,f). WI13 further hypothesized that time-dependent freezing of available active INPs is the source for continuous ice nucleation and precipitation in such supercooled, long-lived layer clouds. We will test this hypothesis with different sensitivity tests in section 5.

### 2) RECIRCULATION OF DUST PARTICLES INTO SUPERCOOLED LAYER CLOUDS (APPRAISE)

Figure 9 shows the time–height profiles of various microphysical properties for the APPRAISE case (also see Fig. 1 in the online supplement). From Figs. 9a and 9b, it is evident that liquid and ice coexist at all levels in the episodes of weak embedded convection ( $\sim 0000$ – $1200$  UTC) of the simulation

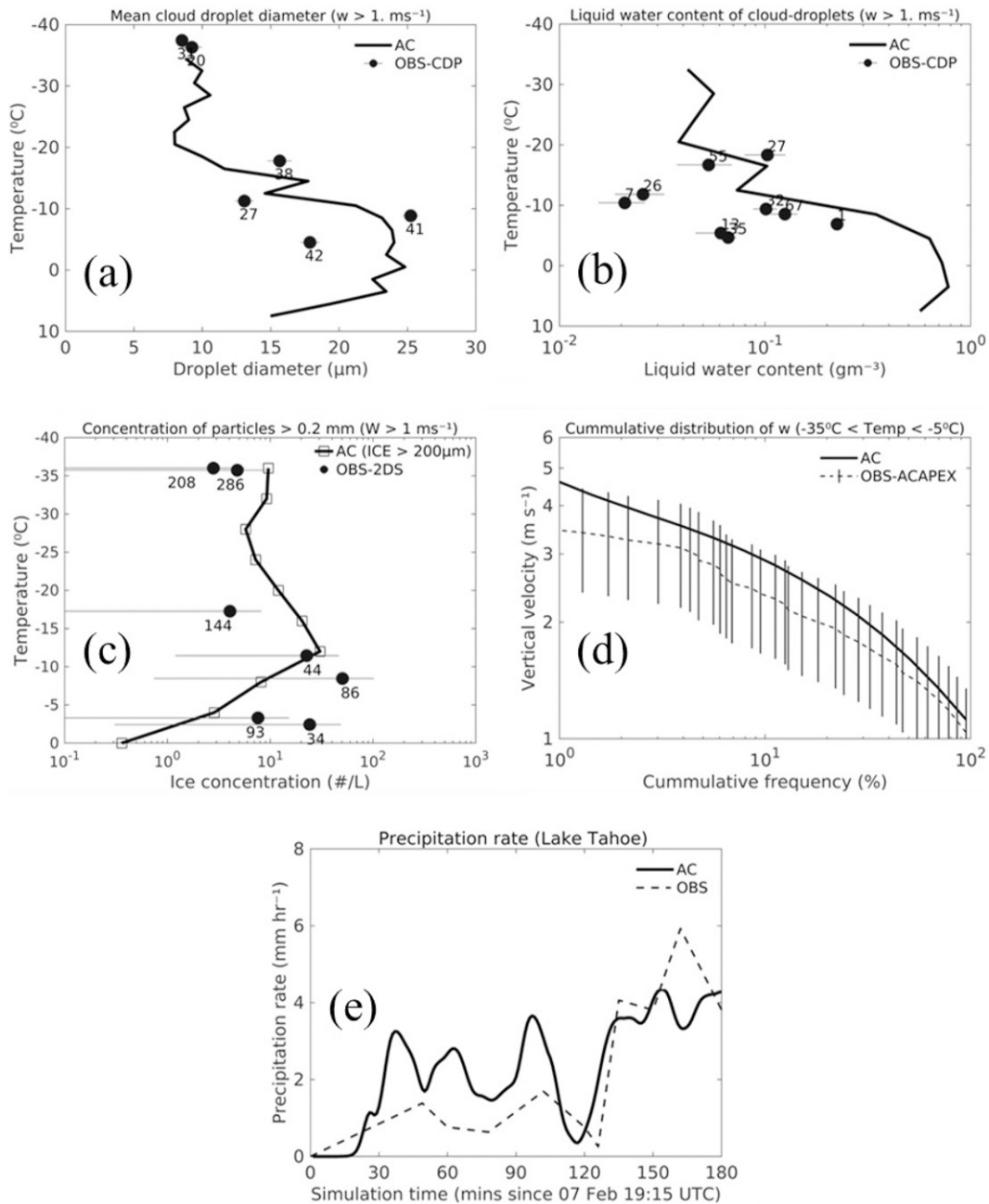


FIG. 6. Conditionally averaged predictions from the control simulation of the simulated ACAPEX case over regions of convective cloudy updrafts ( $w > 1 \text{ m s}^{-1}$ ) for (a) mean cloud droplet diameter (solid black line) and (b) LWC (solid black line) from the control simulation compared with the CDP observations (circles). (c) 2DS-measured ice concentrations for particles  $> 0.2 \text{ mm}$  ( $N_{I200}$ ) compared with the predicted ice concentrations ( $> 0.2 \text{ mm}$ ) for all microphysical species (cloud ice, snow, and graupel/hail) in such updrafts. (d) Histogram of predicted vertical velocities ( $w > 1 \text{ m s}^{-1}$ ) with observations from the DOE G-1 aircraft and (e) predicted surface precipitation rate ( $\text{mm h}^{-1}$ ) from the control simulation with observations from a rain gauge located at Lake Tahoe, California, United States. Standard errors of observational samples are shown as error bars in (a)–(d). Numbers by observation data points in (a)–(c) indicate the time in seconds for which the aircraft sampled the cloud at that level.

(Figs. 7e,g). As the simulation advances in its second half ( $\sim 1200\text{--}2400 \text{ UTC}$ ), supercooled layer clouds are seen (Figs. 7f,h). These clouds are characterized by a thin ( $\sim 400 \text{ m}$  vertical extent) cloudy layer (Fig. 9a) at levels between the cloud top

( $-13^{\circ}\text{C}$ ) and  $-7^{\circ}\text{C}$ . Below  $-7^{\circ}\text{C}$ , the atmosphere is subsaturated ( $\text{RH} < 70\%$ ) up to about  $0^{\circ}\text{C}$  (Fig. 9g). At levels warmer than  $0^{\circ}\text{C}$ , the air was saturated with respect to water (Figs. 3c and 9a). This water-saturated layer at lower levels

resulted in the formation of boundary layer stratiform clouds ( $\sim 1$  km thick) lasting about a day. By contrast, in the early simulation hours (0000–1200 UTC), the atmosphere was nearly saturated. Furthermore, these predicted weak convective and supercooled layer clouds are characterized by an ascent speed of about  $1 \text{ m s}^{-1}$  and less than  $0.6 \text{ m s}^{-1}$  (Fig. 9i), respectively, with continuous precipitation over several hours (Fig. 9h).

Consequently, we analyze how the quasi-steady state is maintained in the fixed domain for supercooled layer clouds over several hours. Figure 9a shows a layer of mixed-phase cloud continuing for about half a day between  $-7^\circ$  and  $-13^\circ\text{C}$ . It is predicted that cloud droplets from this mixed-phase layer fall, and the smaller of these droplets may evaporate once they enter the region subsaturated with respect to both liquid and ice (Fig. 9g), releasing dust particles embedded in them. Moreover, at cloud-top levels, dust INPs initiate ice crystals and some of these crystals may grow to snow following vapor diffusion or aggregation. These ice (crystals and snow) particles may fall and some of them may sublimate away once they reach the subsaturation region. It is predicted that in the subsaturated environment, evaporation of droplets and sublimation of snow releases dust particles embedded in them, which form about 45% and 10% of the total dust mass, respectively, there. This is evident from Fig. 9c which shows that in the subsaturated environment, the upward mass flux [ $\sim 10^{-11} \text{ kg m}^{-2} \text{ s}^{-1}$  (a particle flux of about  $10^4 \text{ m}^{-2} \text{ s}^{-1}$ )] of dust particles in the air is higher by about a factor of 5 than in the cloudy layer (e.g., near cloud top, Fig. 9e). This can be mainly attributed to evaporation of cloud droplets at subsaturated levels ( $0^\circ$  and  $-7^\circ\text{C}$ , Fig. 9g), that releases dust particles embedded in them followed by an ascent in weak vertical motions (e.g., turbulence or weak convective cells), as simulated by AC.

## 5. Results from sensitivity tests in the simulated clouds

To evaluate the role of time dependence for heterogeneous ice nucleation, various sensitivity tests have been performed with AC (Table 3). These involved perturbation simulations from altering the control run in each of the three cases. Comparison with the control simulation revealed the effects from each prohibited process of ice initiation.

### a. Role of time dependence of INP activity in overall ice production

Figure 10 shows the predicted number concentrations of active INPs, total and primary ice, and ice from various SIP processes in the stratiform regions ( $|w| < 1 \text{ m s}^{-1}$ ) with time-dependent INP activity prohibited (the “no time-dependent INP” run) for all three cases (section 2). These are compared with the three corresponding control runs that include this time dependence. These components of ice concentration were tracked by tagging tracers (section 3). Average number concentrations of active dust INPs are predicted to increase by a factor of 2 for the deep convective case (MC3E) and by about 0.5–1 order of magnitude for both layer-cloud cases (APPRAISE and ACAPEX), depending on the level (Figs. 10a,c,e) with inclusion of time dependence.

Also, active soot INPs show a similar sensitivity. However, active dust INPs are the most sensitive out of all the simulated INP species in this regard and have the maximum effect on the overall primary ice initiation. The same order-of-magnitude (0.5–1) increase is predicted also for the tagged concentrations of heterogeneously nucleated ice at colder levels ( $< -7^\circ\text{C}$ ) (Figs. 10a,c,e). The greater time dependence of INP activity in the layer-cloud cases (ACAPEX and APPRAISE) is due to longer lifetimes of such clouds with weaker ascent (Houze 2014), allowing more time for INPs to activate than in the convective case (MC3E).

In the APPRAISE control simulation of mixed-phase layer clouds in a frontal system, most of the primary ice is initiated by dust and soot INPs near cloud top ( $-13^\circ\text{C}$ ). The fractional increase in number concentrations of dust INPs from inclusion of time dependence has a maximum of about an order of magnitude at about  $-6^\circ\text{C}$  (Fig. 10e). Yet the total ice concentration in such stratiform clouds is predicted to increase by only a factor of 2 between  $-4^\circ$  and  $-8^\circ\text{C}$  in the control run relative to the “no time-dependent INP” run (Fig. 11f).

The weakness of this overall response of the cloud glaciation in APPRAISE is due to various SIP mechanisms, especially through the HM process and fragmentation in ice–ice collisions. Between  $0^\circ$  and  $-7^\circ\text{C}$ , SIP mechanisms are predicted to create an ice enhancement (IE) ratio as high as  $10^2$  in the control run, greatly suppressing the response to time dependence of primary ice. However, in such thin clouds (APPRAISE,  $\sim 3$  km in depth), SIP is less active than in the other two simulated cases (section 4b). At levels colder than  $-10^\circ\text{C}$  where the heterogeneous ice nucleation occurs, there is an IE ratio of only about 3. This weak SIP is nevertheless sufficient again to reduce the response of total ice concentrations to the boosting of primary ice from time dependence of freezing INPs, with only a doubling of total and secondary ice concentrations.

By contrast, in the MC3E and ACAPEX clouds, no significant change in total ice concentrations is predicted from the inclusion of time dependence. This too can be attributed to various SIP processes dominating total ice initiation in both the simulated cases at all levels warmer than the  $-36^\circ\text{C}$  isotherm. Both cases involved deeper clouds with more intense precipitation through ice-crystal process driving more vigorous SIP. Vertical profiles (Figs. 10b,d) of average concentration of ice particles from various initiation processes reveal that all SIP (section 3) initiates more than 99% and 90% of total nonhomogeneous ice (not from homogeneous freezing) at most levels warmer than the  $-36^\circ\text{C}$  in MC3E and ACAPEX, respectively. At levels colder than  $-8^\circ\text{C}$ , fragmentation in ice–ice collisions is the most prolific ( $>75\%$  of the total nonhomogeneous ice concentration) SIP mechanism in both cases (MC3E and ACAPEX). The HM process is also active at temperatures between  $-3^\circ$  and  $-8^\circ\text{C}$ , contributing about 85% to the total nonhomogeneous ice but only at these levels. Furthermore, fragmentation during raindrop freezing and sublimation together is predicted to contribute  $\sim 10\%$  to the total nonhomogeneous ice initiated at levels colder than  $-15^\circ\text{C}$ . In the ACAPEX simulation, fragmentation during sublimation is the second most dominant SIP mechanism in

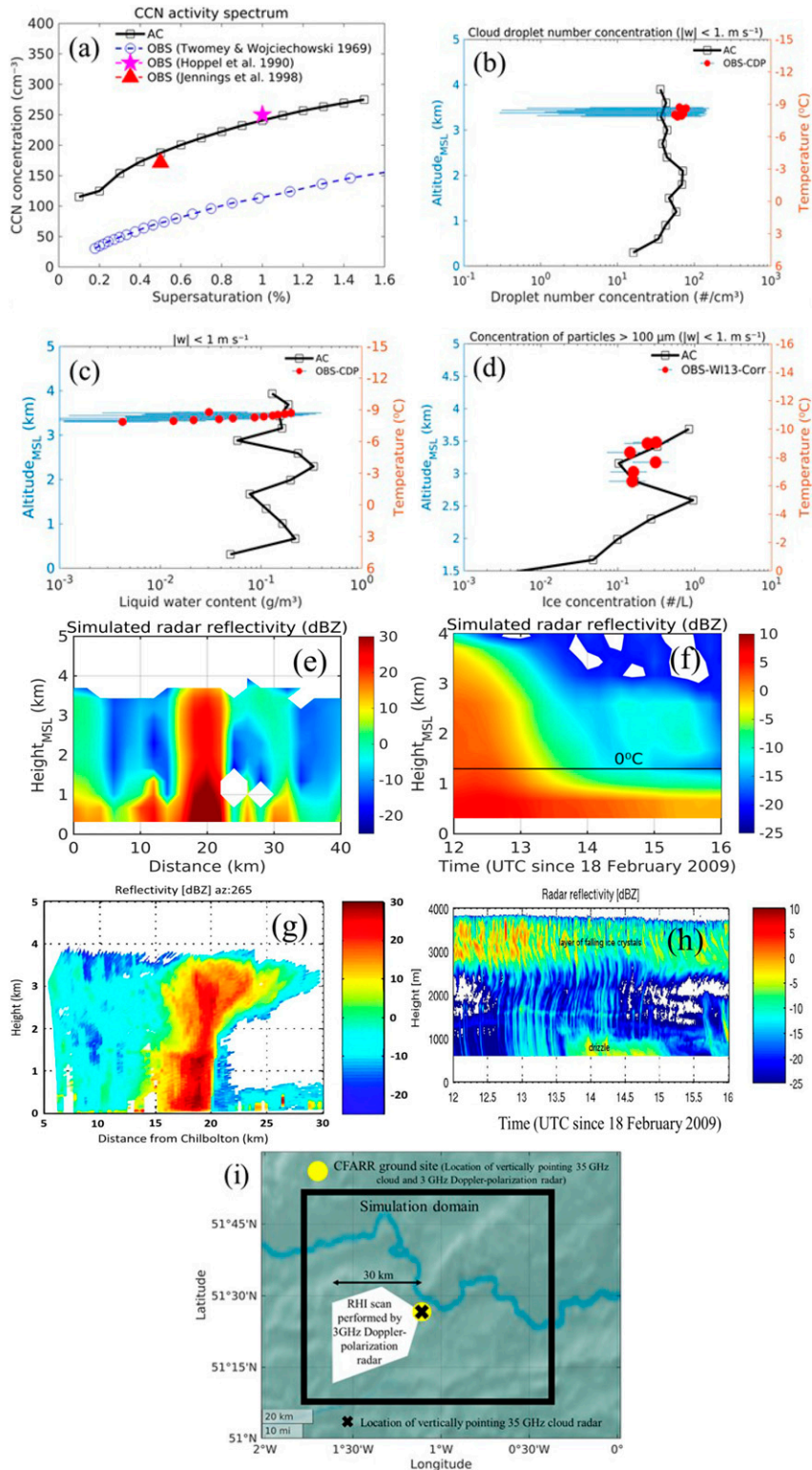


FIG. 7. (a) The CCN activity spectrum predicted by AC (solid black line) for the simulated APPRAISE case (18 Feb 2009) for the environment at about 100 m MSL from the prescribed vertical profiles of size distributions of various aerosol species. This is compared with maritime measurements made by Twomey and Wojciechowski (1969) (open circles), Hoppel et al. (1990) (pentagram), and Jennings et al. (1998), the geometric mean of observations shown in

downdraft regions (not shown here) in both cases. Similar results are predicted in the updraft and downdraft convective regions separately as for the stratiform regions for each of the simulated MC3E and ACAPEX cases (not shown here).

Regarding the time evolution at the lowest subzero levels ( $-2^{\circ}$  to  $-10^{\circ}\text{C}$ ) in layer cloud, Fig. 11 shows concentrations of ice particles conditionally averaged over all stratiform cloudy regions in the first 3 h after the onset of convection. Regarding the two deeper cloud cases (MC3E and ACAPEX), at times less than about 15 (in MC3E, Fig. 11a) and 40 min (in ACAPEX, Fig. 11b) after the onset of ice, the HM process is the only prolific SIP mechanism, creating IE ratios of about  $10^2$  during these times. The HM process is the most prolific SIP mechanism throughout the lifetime of the ACAPEX layer clouds. Later, as the deep convective cloud tops ascend through the mixed-phase region, fragmentation in ice–ice collisions becomes the most prolific SIP mechanism eventually in MC3E, creating IE ratios as high as  $10^3$  (Figs. 11a,b). This illustrates how fragmentation in ice–ice collisions tends to be slower but more persistent and prolific than the HM process in deep convection (Wa22, their Fig. 18). The ice concentrations in the simulated MC3E and ACAPEX cases reach their maxima after about 20 min, then become quasi steady for the rest of the lifetime of the clouds. Fragmentation during raindrop freezing and sublimation is predicted to form only about 5% of the total nonhomogeneous ice concentrations in all three cases.

Regarding these lower levels in the thin APPRAISE layer clouds (Fig. 11c), the HM process is predicted always to prevail ( $>150$  min) in overall ice concentrations, creating sustained IE ratios as high as  $10^2$ . About 40 min after the onset of convection, heterogeneous ice nucleation become the second most prolific type of ice initiation but forms only about 10% of the total nonhomogeneous ice concentrations between 40 and 100 min. Fragmentation in ice–ice collisions is active but has such a slow rate of explosive growth, owing to lack of ice precipitation, that it only contributes appreciably to the SIP at much longer times than those plotted (Fig. 11c).

Figure 12 shows a budget of ice particles initiated by various processes of ice initiation represented in AC (sections 3a and 3b), showing their contribution to the total ice at levels warmer

than the  $-36^{\circ}\text{C}$  in the control and “no time-dependent INP” simulation (pie charts). The budget analysis shows that in all simulated cases (MC3E, ACAPEX, and APPRAISE), the number of heterogeneously nucleated ice crystals initiated increases by about 30% with a maximum of 45% (in APPRAISE) in the control simulation relative to the “no time-dependent INP” run (Fig. 12a).

The budget analysis also indicates that in all three simulated cases, SIP dominates overall ice production. In the APPRAISE clouds (Figs. 12a,b), fragmentation during ice–ice collisions and sublimation together with the HM process, are predicted to produce about 80% more fragments than those from heterogenous ice nucleation. In the MC3E (Figs. 12c,d) and ACAPEX simulations (Figs. 12e,f), fragmentation during ice–ice collisions and sublimation together initiate more than 95% of the total fragments implying an IE ratio of about  $10^3$ . The budget analysis suggests that fragmentation in sublimation accounts for most of the fragments, creating IE ratios as high as  $10^2$ . However, vertical profiles of tagging tracers (Fig. 10) reveal that fragmentation in sublimation is less prolific than fragmentation in ice–ice collisions (at levels colder than  $-15^{\circ}\text{C}$ ) and the HM process (between  $-3^{\circ}$  and  $-8^{\circ}\text{C}$  levels). This is mainly attributed to the total sublimation of the vast majority ( $>80\%$ ) of fragments initiated during the fragmentation in sublimation while descending.

To summarize, in all the simulated cases (MC3E, ACAPEX, and APPRAISE), the overall ice initiation is mostly dominated by various SIP mechanisms. Little effect ( $<0.01\%$ ) on overall ice concentrations is predicted to arise from time-dependent INP activity.

#### b. Sources of quasi-steady precipitation in APPRAISE clouds

As discussed in sections 4a and 4b(1), our simulation for the APPRAISE case predicts two types of episodes during the evolution of the entire cloud system. First, weak embedded convection episode consisting of thermals with ascent of up to  $1\text{ m s}^{-1}$  (section 4a). Second, long-lived layer-cloud episode, partly from convective outflow of the first episode, for which the stratiform ascent is only a few centimeters per second (section 4a). Both the episodes are predicted to be

---

←  
 their Fig. 1; upward-pointing triangle). Comparison of predicted (b) droplet number concentrations (solid black line), (c) LWC (solid black line) with observations from the CDP, and (d) ice number concentrations for particles of maximum size dimension  $> 100\ \mu\text{m}$  ( $\text{NI}_{100}$ ) of all microphysical species (solid black line) with aircraft observations (circles) from the 2DS probe (adopted from WI13 and corrected following K11), conditionally averaged for the stratiform regions ( $|w| < 1\text{ m s}^{-1}$ ). (e) Snapshot of the simulated radar reflectivity for the APPRAISE case compared with the observations from (g) 3 GHz Doppler-polarization radar at the CFARR ground site, which performed a range–height indicator scan along the  $253^{\circ}$  (adopted from C11) for the episodes of weak embedded convection, and (f) a time–height profile of the simulated radar reflectivity during the episodes of supercooled, long-lived layer clouds compared with the observations from (h) the 35GHz vertical pointing radar at the CFARR (adopted from C11). (i) Schematic diagram showing a view of the simulation domain (black box), the location of the vertically pointing 35 GHz cloud radar (black cross) and the area scanned by 3GHz Doppler-polarization radar located at CFARR ground site (yellow circle). Error bars in (b)–(d) are standard errors of observational samples.

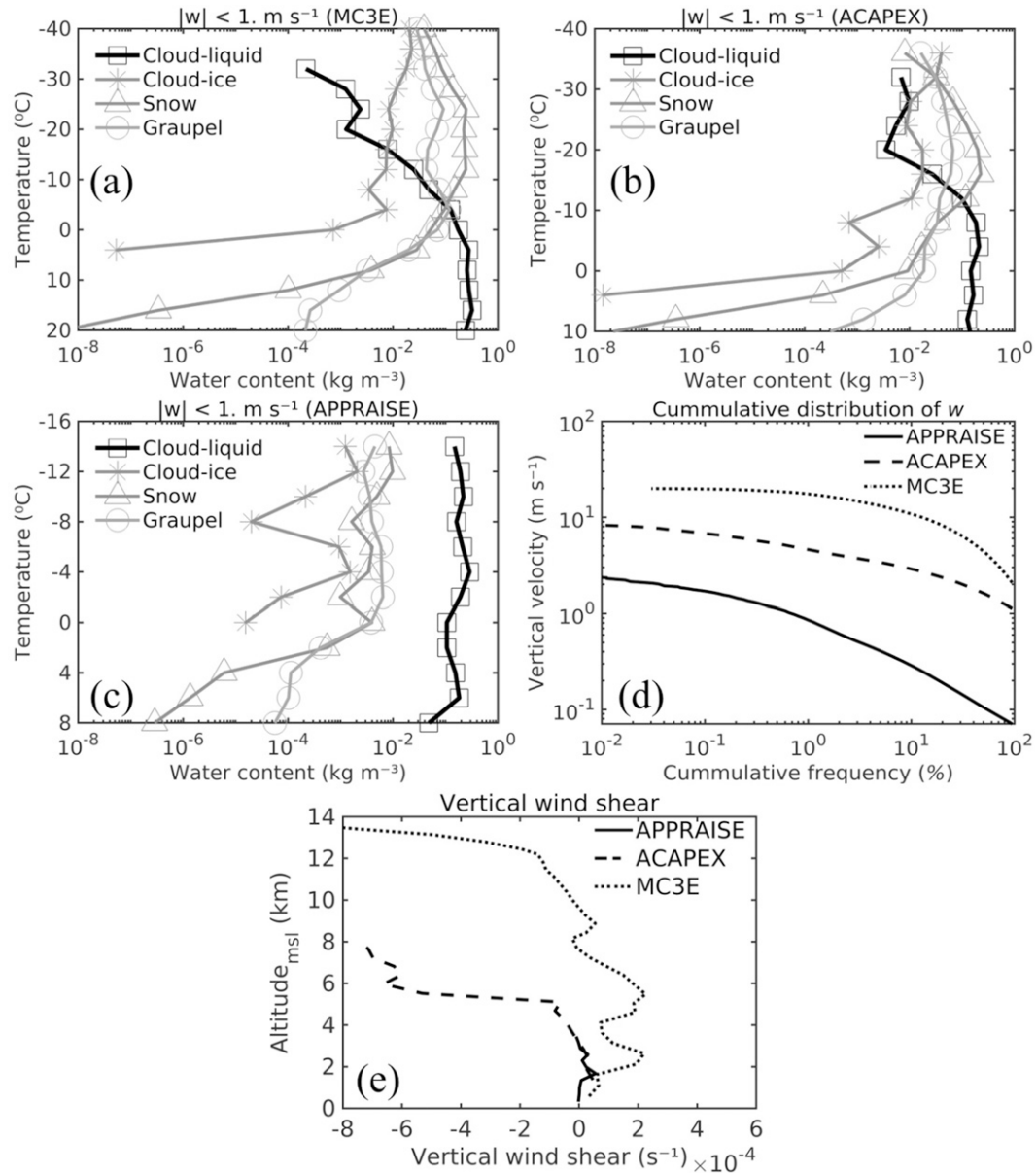


FIG. 8. The predicted water contents of cloud liquid (squares), cloud ice (asterisks), snow (upward-pointing triangles), and graupel (circles) in the stratiform regions ( $|w| < 1 \text{ m s}^{-1}$ ) from the control simulations of the (a) MC3E, (b) ACAPEX, and (c) APPRAISE cases. Also shown are (d) a vertical velocity histogram and (e) a profile of vertical wind shear from the control simulation of the APPRAISE (solid line), ACAPEX (dashed line), and MC3E (dotted line) cases.

precipitating continuously over several hours (Fig. 9h). However, ice initiation mechanisms influencing precipitation are predicted to differ between both types of episodes, as follows.

#### 1) ICE INITIATION DURING THE WEAK EMBEDDED CONVECTION EPISODE

Figure 13 shows the total ice concentration (black lines) with time-dependent activity prohibited in the stratiform regions ( $|w| < 1 \text{ m s}^{-1}$ ) of the weak embedded convection

episode ( $\sim 0000\text{--}1200 \text{ UTC}$ , section 4a) in comparison with the control run. In such clouds, the inclusion of time dependence causes only a slight increase ( $\sim 30\%$ ) in the overall ice concentrations in the control simulation. This is because SIP is predicted to initiate about 75% of the total ice concentration at all subzero cloudy levels over several hours there. A similar extent of SIP was observed by C11 (their Fig. 11), attributing it to the HM process. In the control simulation, the HM process ( $-3^\circ$  to  $-8^\circ\text{C}$ ) and fragmentation in ice-ice collisions ( $< -8^\circ\text{C}$ ) contribute about 75% and 80%, respectively,

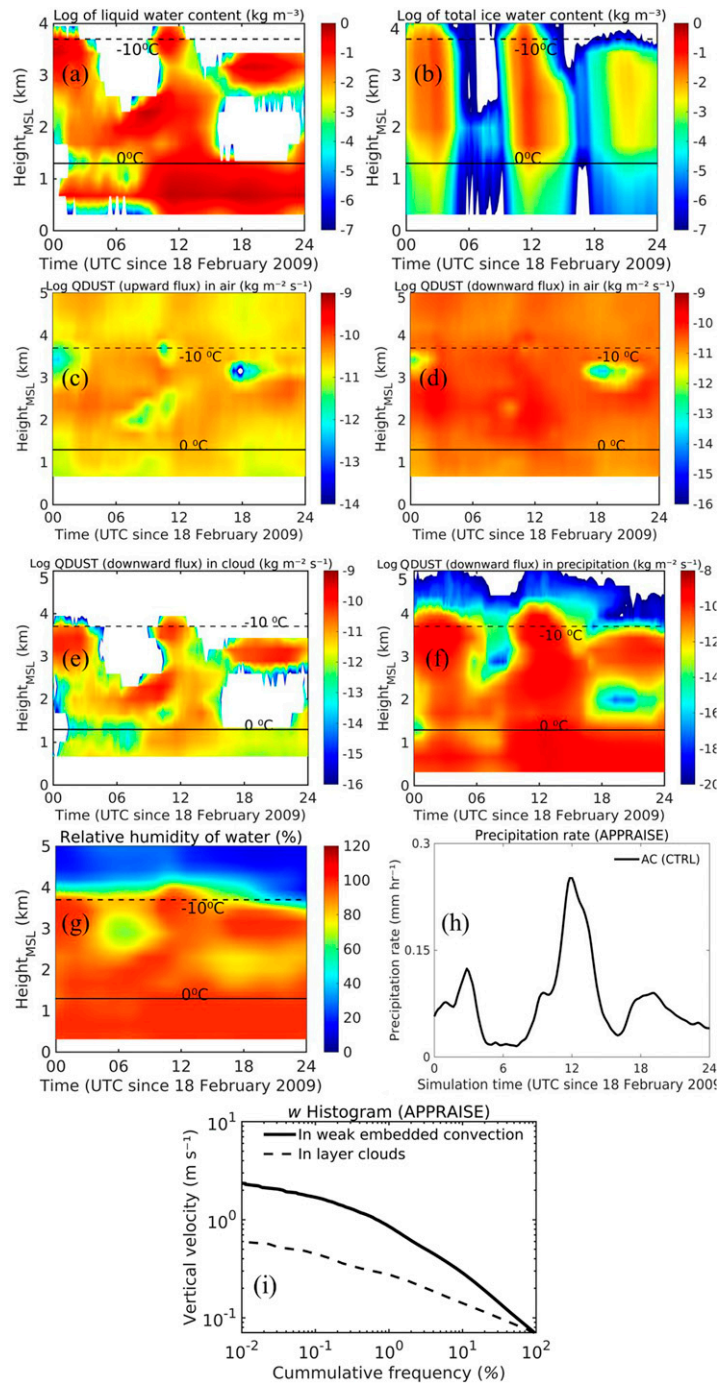


FIG. 9. Time–height profiles of the domain-averaged water contents of (a) cloud liquid, (b) total ice (cloud ice + snow + graupel), and (c) upward and (d) downward fluxes of the mass mixing ratio of dust particles in the air, and downward mass flux of dust mixing ratio in (e) cloud, and (f) precipitation, and (g) relative humidity with respect to water from the control simulation of the APPRAISE case between 0000 and 2400 UTC 18 Feb 2009. Also shown are the (h) precipitation rate, and (i) a vertical velocity histogram for the regions of weak convective cells (solid line) and supercooled layer clouds (dotted line) from the same simulation. All the quantities in (a)–(f) are plotted in log scale.

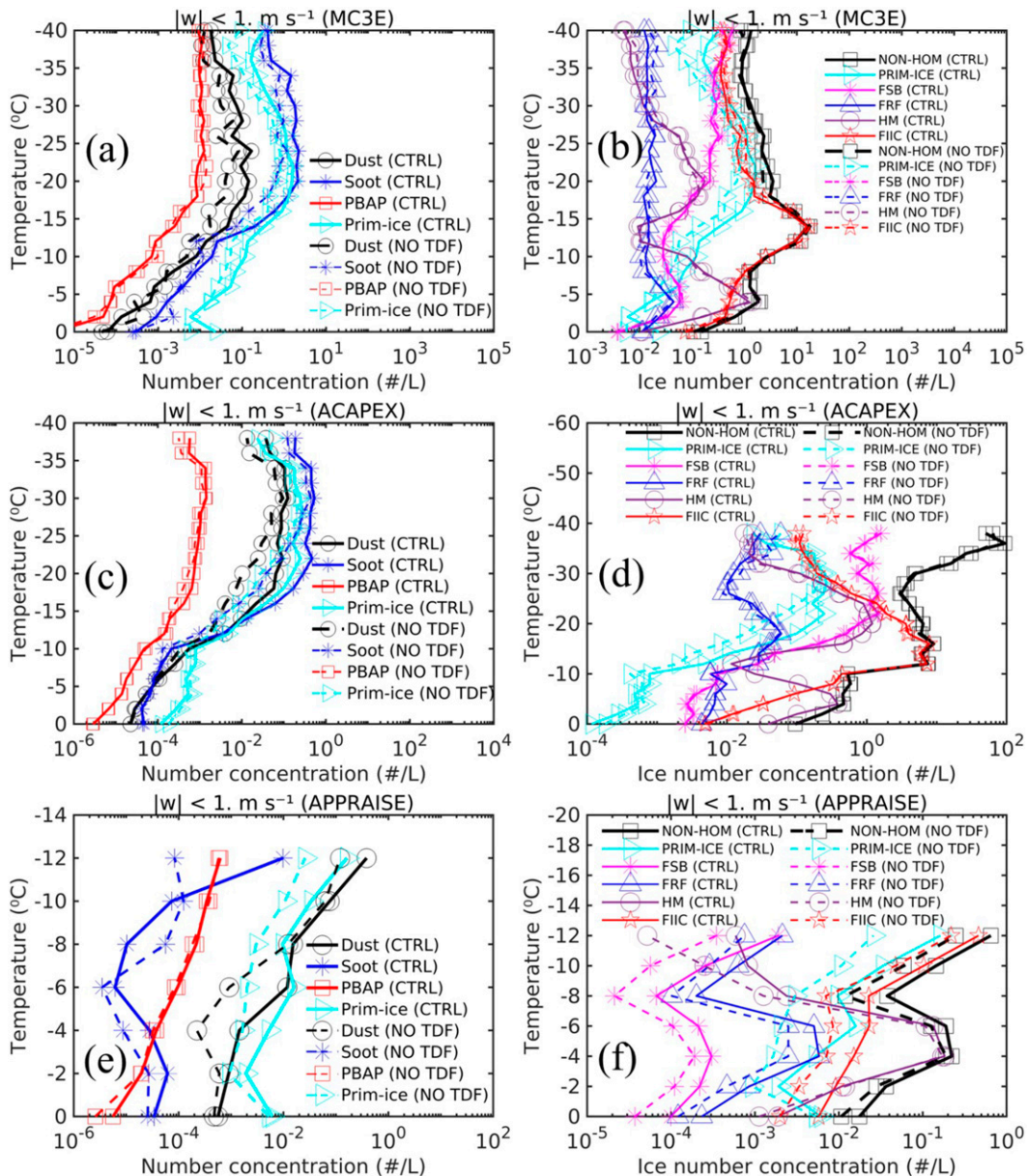


FIG. 10. (left) The predicted number concentrations of active INPs conditionally averaged over stratiform regions ( $|w| < 1 \text{ m s}^{-1}$ ) from mineral dust (solid line with open circles), soot (solid line with asterisks), and PBAP (solid line with squares), and concentrations of heterogeneously nucleated ice (PRIM-ICE, forward-pointing triangles) for the (a) MC3E, (c) ACAPEX, and (e) APPRAISE cases. The same information is shown with dotted lines for the “no time-dependent INP” run. (right) The concentrations of total nonhomogeneous ice (total cloud ice and snow minus total homogeneous ice; solid line with squares) and various tracer terms defining SIP processes such as fragmentation during sublimation (FSB; solid line with asterisks), ice-ice collisions (FIC; solid line with pentagrams) and raindrop freezing (FRF; solid line with upward-pointing triangles), and the HM process (HM; solid line with open circles) for the (b) MC3E, (d) ACAPEX, and (f) APPRAISE case, respectively. The same information is shown with the dotted lines for the “no time-dependent INP” run. To compare the number concentrations of heterogeneously nucleated ice and total nonhomogeneous ice, heterogeneously nucleated ice (PRIM-ICE; forward-pointing triangles) is also shown in the right column.

to the total ice concentration (Fig. 13, grayscale lines) during this episode. However, heterogeneously nucleated ice forms only about 10%–20% of the overall ice concentrations (Fig. 13) at these levels.

Nevertheless, in both the control and no time-dependent INP case, ice crystals nucleated heterogeneously at levels near cloud top may become snow by vapor diffusion. This creates a positive feedback of ice multiplication by fragmentation

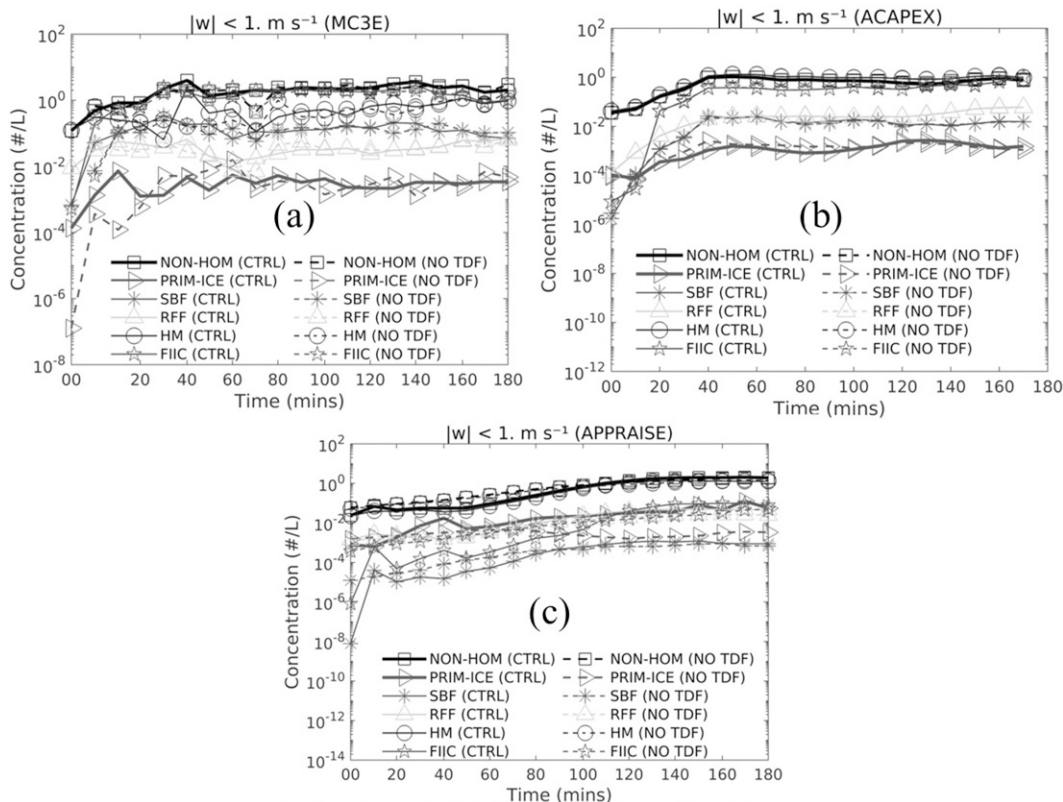


FIG. 11. Domain-averaged distributions with respect to time of the number concentrations of total nonhomogeneous ice (total ice from cloud ice and snow minus total homogeneous ice; squares), primary ice (forward-pointing triangles), and ice (cloud ice + snow) from tagging tracers of various SIP processes such as fragmentation during sublimation (SBF; asterisks), raindrop freezing (RFF; upward-pointing triangles), and fragmentation during ice–ice collisions (FIIC; pentagrams), and from the HM process (HM; circles) from the control simulation of (a) MC3E, (b) ACAPEX, and (c) APPRAISE cases. These concentrations are averaged for vertical velocities  $|w| < 1 \text{ m s}^{-1}$  at temperatures between  $-2^\circ$  and  $-10^\circ\text{C}$ . The same information is shown with dotted lines for the “no time-dependent INP” run. Time displayed is for the time after the first onset of ice.

in ice–ice collisions for up to several hours, causing a peak precipitation rate of about  $0.3 \text{ mm h}^{-1}$  at the surface (Fig. 9h) from the ice–crystal process. Hence, SIP (through the HM process and fragmentation in ice–ice collisions) is predicted to be the main source for the persistence of the weak embedded convection episode of the simulated APPRAISE clouds, which is also shown schematically in Fig. 14a.

In summary, during the weak embedded convection episode, this ice multiplication is promoted by the coexistence of cloud ice, snow, and graupel in proximity (Fig. 8c) and relatively strong vertical velocities ( $|w| \sim 1 \text{ m s}^{-1}$ , Fig. 9i).

## 2) ICE INITIATION DURING THE LONG-LIVED LAYER-CLOUD EPISODE

In this section, focus is given to the duration of the simulation when weak convection is absent and there are only persistent long-lived layer clouds ( $\sim 1200\text{--}2400$  UTC, Fig. 7f) as observed by WI13. Our simulation approximately reproduced the quasi-steady state of the cloud top (Fig. 7h) for the long-lived layer-cloud episode which is consistent with the observations by WI13. The same is true for precipitation (Fig. 9h). WI13 proposed that

in such layer clouds, time-dependent freezing of available INPs is the main cause for continuous ice nucleation and precipitation.

In the long-lived layer-cloud episode, the inclusion of time dependence is predicted to increase the overall ice concentrations by only about 30% at levels near the cloud top ( $-9^\circ$  to  $-13^\circ\text{C}$ ) in the control simulation relative to the “no time-dependent INP” run. In this episode, heterogeneously nucleated ice and SIP (Fig. 15a) forms about 80% and 20% of the overall ice concentrations, respectively, at all subzero levels in the control simulation. A similar extent of heterogeneous ice was observed by WI13. However, contrary to the claim by WI13, time-dependent INP freezing would not be the cause for continuous ice nucleation and precipitation in such layer clouds, as it causes only a slight increase ( $\sim 30\%$ ) in the overall ice production.

It is instead predicted that the recirculation of dust APs [section 4b(2)] is the main cause for the persistence of ice nucleation and precipitation in the long-lived layer-cloud episode. It is evident from Figs. 9c–f that dust APs that become free in droplet evaporation in the subsaturated environment ( $0^\circ$  to  $-7^\circ\text{C}$ , Fig. 9a) reach the saturated cloudy layer ( $-7^\circ$  to  $-13^\circ\text{C}$ , Fig. 9a) following weak vertical motions and can

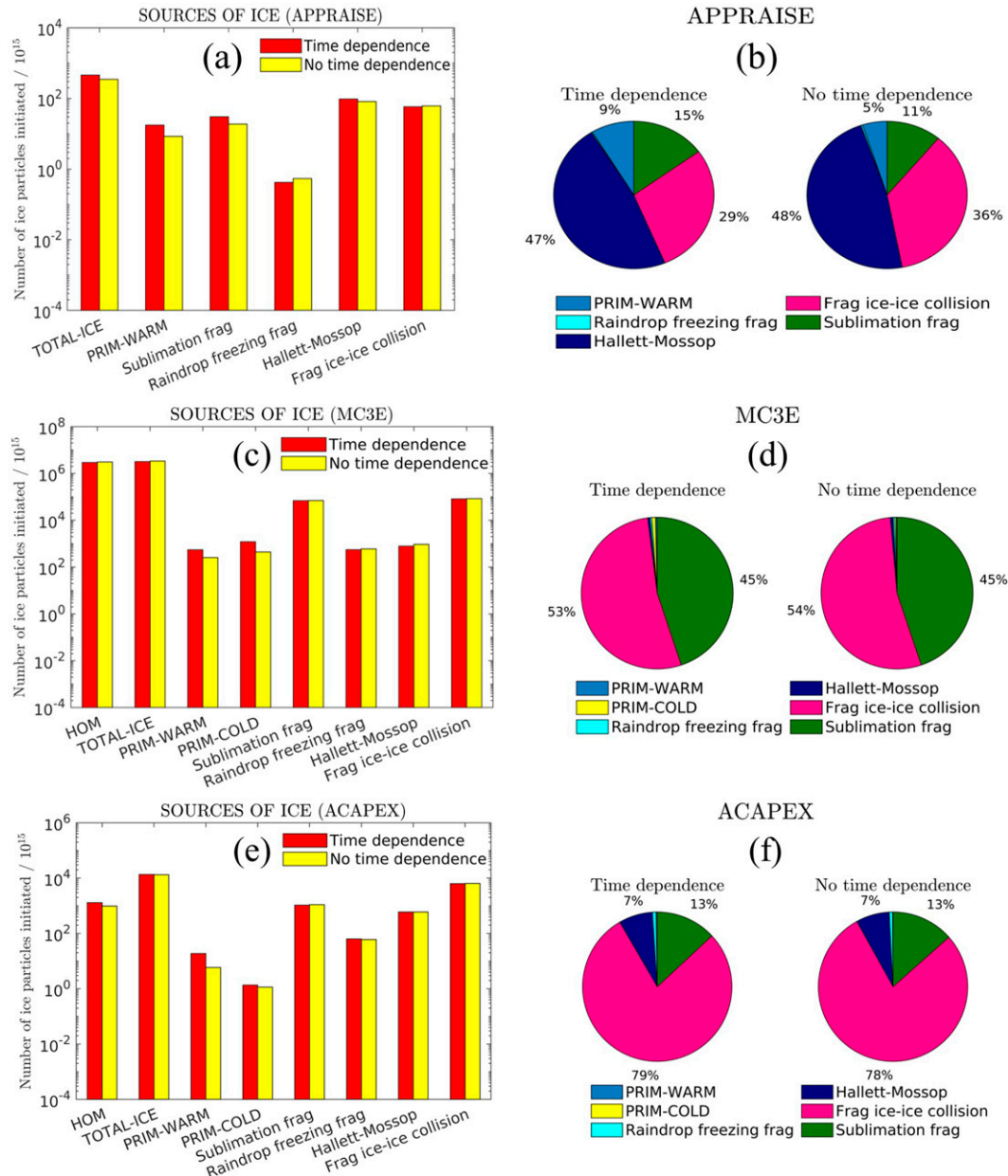


FIG. 12. (left) Bar charts showing a comparison of the budget of the number of ice crystals initiated from primary ice and SIP processes between the control and “no time-dependent INP” run for the (a) APPRAISE, (c) MC3E, and (e) ACAPEX cases. Shown are the sources of homogeneously nucleated ice (“HOM”), total ice from all ice initiation processes (TOTAL-ICE), heterogeneous ice nucleation at temperatures warmer than  $-30^{\circ}\text{C}$  (“PRIM-WARM”) and colder than  $-30^{\circ}\text{C}$  (“PRIM-COLD”), and various SIP mechanisms active. These are fragmentation during raindrop freezing (“Raindrop freezing frag”), ice-ice collisions (“Frag ice-ice collisions”) and sublimation (“Sublimation frag”), and the HM process (“Hallett-Mossop”). (right) The same information is shown (excluding “HOM” and “TOTAL-ICE”) with the pie charts for the simulated (b) APPRAISE, (d) MC3E, and (f) ACAPEX simulations.

reactivate and nucleate ice there. Also, there is a significant downward flux of dust APs from levels above the cloud top (Fig. 9d) which again can initiate ice once a water-saturated cloudy layer is reached.

This reactivation following recirculation of dust APs (Fig. 14b) from the subsaturated environment is predicted to

occur over a time scale (in-cloud dust mass concentration divided by the upward dust mass flux from below) of 1–2 h, which is much less than the time required ( $>10$  h) for their INP activity to increase by about a factor of 10 according to the laboratory observations (Jk22). Furthermore, during this recirculation and reactivation, some of the hydrometeors may

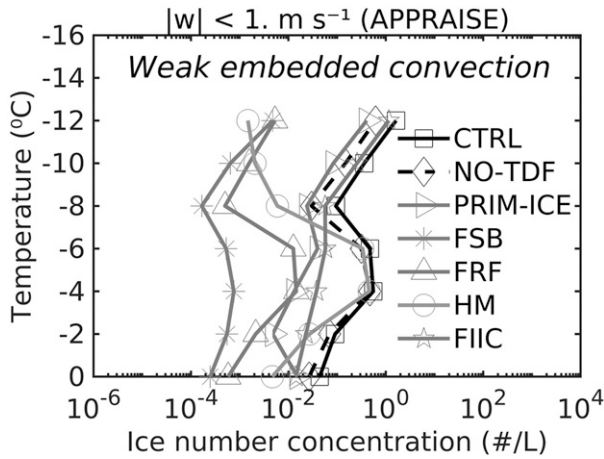


FIG. 13. Predicted number concentrations, during the weak embedded convection episode, of primary (forward pointing triangles) and total nonhomogeneous ice (total cloud ice and snow minus total homogeneous ice) from the control (squares) and “no time-dependent INP” (diamonds) run. Also shown are the ice particle number concentrations from various tracer terms defining SIP processes such as fragmentation during sublimation (FSB; asterisks), raindrop freezing (FRF; upward pointing triangles), and ice–ice collisions (FIIC; pentagrams), and the HM process (HM; circles). All quantities are conditionally averaged over the stratiform regions ( $|w| < 1 \text{ m s}^{-1}$ ), in APPRAISE clouds ( $\sim 0000\text{--}1200 \text{ UTC}$  18 Feb 2009).

survive long enough and enter the liquid cloudy layer (1.2–0.3 km) leading to light precipitation in the form of drizzle or ice (Fig. 14b), as observed by W113.

This is also evident from Fig. 15b which shows that in the long-lived layer-cloud episode, the overall ice concentration

decreases by about an order of magnitude in the “no dust from droplet evaporation” run relative to the control simulation. Hence, in such layer clouds (APPRAISE), it is predicted that reactivation following recirculation of dust APs is the main cause for the observed quasi-steady state of ice nucleation (W113) over several hours, and not time-dependent freezing of available INPs.

6. Summary and conclusions

Three cloud cases have been simulated numerically with AC to investigate the effect from time-dependent INP activity on the total ice concentration. These are 1) an MCS consisting of deep convective clouds observed in MC3E over Oklahoma, United States, on 11 May 2011 (Wa22), 2) orographic stratiform layer clouds with embedded convection observed in ACAPEX over Northern California, United States, on 7 February 2015, and 3) thin, mixed-phase, supercooled stratiform clouds observed in APPRAISE on 18 February 2009 over the southern United Kingdom. All these simulations are validated adequately with coincident aircraft and ground-based observations. In all three simulated cases, cloud droplet properties such as mean droplet sizes, concentrations (in MC3E), and LWC differ no more than 40% from the coincident aircraft observations at most of the sampled levels where data are available.

A striking conclusion is that the filtered ice concentrations ( $NI_{100}$  and  $NI_{200}$ ) predicted by AC are also validated adequately at all sampled levels, differing by less than about a factor of 3 from the aircraft observations, in all three simulated cases. This is true for both the convective (ACAPEX and MC3E only) and stratiform regions of each case. The general realism of representations of all four SIP mechanisms (section 3b) in AC is the reason for the adequate validation of

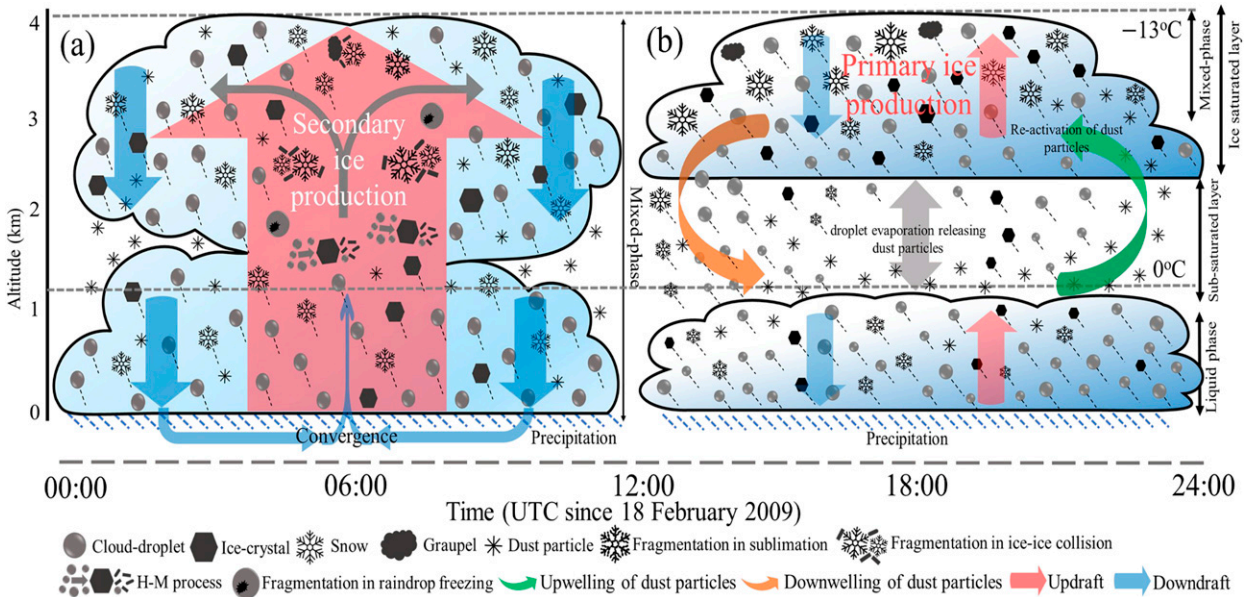


FIG. 14. A schematic of the APPRAISE clouds representing the sources of quasi-steady precipitation from the control simulation in the (a) weak embedded convection episode ( $\sim 0000\text{--}1200 \text{ UTC}$ ) and (b) long-lived layer-cloud episode ( $\sim 1200\text{--}2400 \text{ UTC}$ ) on 18 Feb 2009.

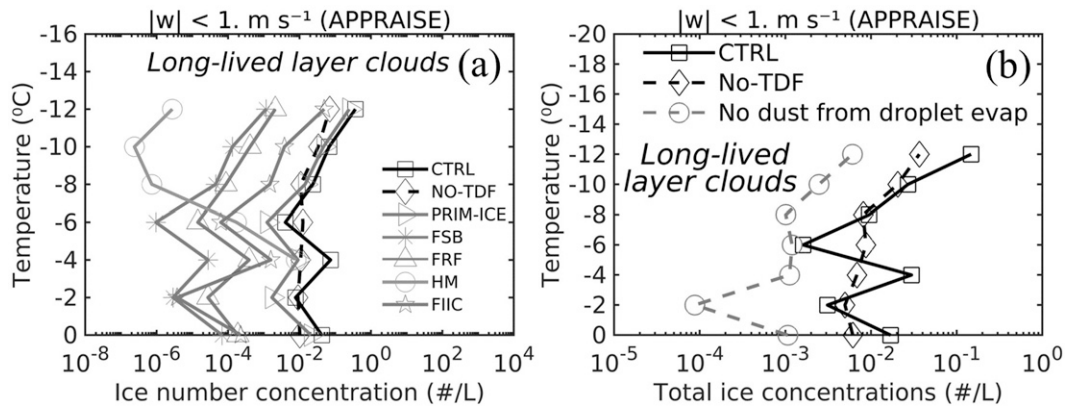


FIG. 15. During the long-lived layer-cloud episode of the APPRAISE case, conditionally averaged predicted number concentrations of the (a) total nonhomogeneous (total cloud ice and snow minus total homogeneous ice) ice from the control (squares) and “no time-dependent INP” (diamonds) run, heterogeneously nucleated ice (forward-pointing triangles), and various tracer terms defining SIP processes such as the Hallett–Mossop process (HM; circles), and fragmentation during ice–ice collisions (FIIC; pentagrams), sublimation of dendritic snow and graupel (FSB; asterisks), and raindrop freezing (FRF; upward-pointing triangles), over the stratiform regions ( $|w| < 1 \text{ m s}^{-1}$ ). Also shown are the total concentrations of nonhomogeneous ice from the (b) control (squares), “no time-dependent INP” (diamonds), and “no dust from droplet evaporation” (circles) simulations of the same clouds.

the number concentration of ice particles. Hence, there is no discrepancy between the observed and predicted ice concentrations as reported in some previous modeling studies (e.g., Fridlind et al. 2007, 2017; reviewed by Field et al. 2017).

Moreover, the vertical profiles of tagging tracers plotted for the control and “no time-dependent INP” runs reveal that the total ice concentrations in all the simulated clouds are mostly driven by ice formed in various SIP processes in all three cases. This is consistent with some previous studies (e.g., Lawson et al. 2015; Lasher-Trapp et al. 2016, 2021; Sotiropoulos et al. 2020; Qu et al. 2023). In all simulated clouds of the present study, fragmentation in ice–ice collisions contributes about 75%–95% to the total ice at most levels warmer than about  $-30^\circ\text{C}$ . At levels between  $-3^\circ$  and  $-8^\circ\text{C}$ , the HM process initiates most of the ice particles ( $\sim 70\%$ ) in the ACAPEX and APPRAISE simulations.

The budget analysis shows that the time dependence of INP activity makes no significant contribution ( $<10\%$ ) to the total number concentrations of ice particles initiated from all the processes in orographic and MCS clouds warmer than the  $-36^\circ\text{C}$  level (MC3E, ACAPEX). In such clouds, fragmentation during ice–ice collisions (in updraft and stratiform regions) and during sublimation (in downdrafts only, counting fragments that survive) initiates more than 70% of the total ice particles. Consequently, the time dependence of INPs has little effect. In the case of the APPRAISE clouds, overall, the time dependence of INP activity is predicted to contribute about 30% of the total number of ice particles initiated, while SIP mechanisms active in such clouds initiate 70% of the total ice particles.

The conclusions of the present study are as follows:

- 1) Generally, for the total ice in precipitating clouds, the inclusion of time dependence is predicted to initiate about 10% of the total ice warmer than the  $-36^\circ\text{C}$  level,

whereas SIP mechanisms active in such clouds initiate more than 90% of the total ice at these levels in the mixed phase region ( $0^\circ$  to  $-36^\circ\text{C}$ ).

- 2) In all three cases, for INP activity, including time dependence is predicted to have more impact for mineral dust and soot APs than for the other INP APs. This is consistent with the previous laboratory observations (Wright and Petters 2013; Herbert et al. 2014; JK22). The INP activity of mineral dust and soot is predicted to increase by a factor of about 10 and 5, respectively, in the control simulation compared to the “no time-dependent INP” run at temperatures between  $-5^\circ$  and  $-25^\circ\text{C}$ . The least (only a factor of 2) increase is seen for PBAP groups from the inclusion of the time-dependent INP activity.
- 3) Specifically, in the simulated MCS (MC3E) system,
  - (i) Overall, enhancement by a factor of up to about 4 (from dust APs) is seen in heterogeneously nucleated ice, whereas the total ice concentration is predicted to increase by only a factor of about 2 at levels colder than  $-15^\circ\text{C}$  in all cloudy regions in the control run relative to the “no time-dependent INP” run.
  - (ii) Regarding SIP, in updrafts, the HM process contributes about 30% to the total ice concentration at levels between  $-3^\circ$  and  $-8^\circ\text{C}$ , while this contribution is less ( $<10\%$ ) in the convective downdraft and stratiform regions. In the convective updraft and stratiform regions, fragmentation in ice–ice collisions is the most prolific SIP mechanism at levels colder than  $-8^\circ\text{C}$  and initiates about 80% of the total ice at those levels. Fragmentation during sublimation is mostly active in stronger downdrafts ( $w < -5 \text{ m s}^{-1}$ ), initiating more than 15% of the total ice. All this SIP is far less sensitive to time-dependent INP activity than is primary ice itself.

- 4) In the case of orographic (ACAPEX) clouds,
  - (i) Concentrations of heterogeneously nucleated ice are about half an order of magnitude higher in the control simulation relative to the “no time-dependent INP” run in all cloudy conditions. The same is true for the number concentrations of active dust INPs. However, no change is seen in the total ice concentration when the time dependence of INP activity is included.
  - (ii) The HM process is the most prolific SIP mechanism at levels between  $-3^{\circ}$  and  $-8^{\circ}\text{C}$  and initiates more than 80% of the total ice concentration there in all cloudy conditions. In convective updrafts, fragmentation during ice–ice collisions contributes about 50% to the total ice concentration at levels colder than  $-15^{\circ}\text{C}$ . While in convective downdrafts, fragmentation in sublimation is predicted to be more prolific and initiates about 40% of the overall ice concentration at these levels. Again, in this case, SIP acts to dampen the sensitivity of time dependence of INP activity.
- 5) In thin, long-lived mixed-phase stratiform (APPRAISE) clouds,
  - (i) Overall, the total ice concentration is predicted to be about a factor of 3 higher, while the heterogeneously nucleated ice is about an order of magnitude higher, at all subzero levels when time dependence of INP activity is included.
  - (ii) In the weak embedded convection episode, SIP (through the HM process and fragmentation ice–ice collisions) forms about 75% of the total ice concentration at all subzero levels, whereas in the long-lived layer-cloud episode, heterogeneously nucleated ice dominate ( $\sim 80\%$ ) overall ice concentration.
  - (iii) In the long-lived layer-cloud episode, it is predicted that the evaporation of droplets in the subsaturation region ( $0^{\circ}$  to  $-7^{\circ}\text{C}$ ) releases dust APs embedded in them, which forms about 45% of the total dust mass there. These released dust APs reactivate and nucleate ice once the mixed-phase cloudy layer ( $-7^{\circ}$  to  $-13^{\circ}\text{C}$ ) is reached following weak vertical motions. Furthermore, dust APs from levels above the cloud top also initiate ice once a saturated cloud layer is reached (Fig. 9d).
  - (iv) This recirculation and reactivation of dust particles in the long-lived layer-cloud episode is predicted to happen over 1–2 h, which is much less than the times required for time-dependent INP freezing to alter the simulated ice concentrations appreciably ( $>10$  h, Figs. 9 and 10).
  - (v) Hence, the recirculation of dust APs back into the cloud from the subsaturated environment is the main reason for the simulated persistence of ice initiation and precipitation production in the long-lived layer-cloud episode, and not time-dependent freezing of available INPs, as claimed by WI13.
- 6) During the evolution of the simulated clouds (section 2) for tops warmer than  $-15^{\circ}\text{C}$  in the stratiform regions

( $|w| < 1 \text{ m s}^{-1}$ ), the initial (times  $< 20$  min) explosive growth of numbers of ice crystals is from the fast HM process. Immediately after 20 min, this explosive growth is continued by fragmentation in ice–ice collisions, which prevails over a longer period. The effect of time dependence remains similar throughout the simulation.

In the simulated MC3E and ACAPEX clouds, SIP is predicted to dominate the overall ice concentrations at all levels colder than  $-36^{\circ}\text{C}$ , whereas heterogeneously nucleated ice makes a negligible contribution ( $<1\%$ ) to the total ice concentration at these levels. This is mainly attributed to the relatively shorter lifetime of such clouds (60–90 min) and the presence of abundant large drops, snow, and graupel particles (Fig. 8) in association with strong convective ascent and descent ( $|w| > 1 \text{ m s}^{-1}$ ) in such clouds, which favor SIP at these levels.

By contrast, in the APPRAISE simulation of a thin layer cloud, the weakness and shallowness of the ascent ( $|w| < 1 \text{ m s}^{-1}$ , Fig. 8d) causes less abundance ( $<10\%$  of the total ice particles) of large snow and graupel particles than the other two (MC3E and ACAPEX) cases. Nevertheless, SIP is still predicted to prevail in overall ice initiation in the episodes of weak convection of this case (APPRAISE), albeit less prolifically than in the other two cases, and initiates about 75% (HM process and fragmentation in ice–ice collisions) of the total ice at all subzero levels there. Generally, treatment of ice initiation through various SIP processes has some uncertainty due to the incompleteness of laboratory studies (e.g., Field et al. 2017) and depends upon various parameters such as particle sizes, vertical velocities, temperature, and hydrometeor fall speed. Hence, the relative roles of various SIP processes in forming high ice concentrations differ among contrasting cloud types.

The present study generally finds little effect from time-dependent ice nucleation on the total ice concentration in a range of cloud types (deep convective, orographic, and long-lived stratiform clouds). In the case of thin, stratiform clouds (APPRAISE) there is at most a doubling of the average concentration of ice particles at levels colder than  $-8^{\circ}\text{C}$  from the inclusion of time dependence. Thus, time dependence alone cannot predict the observed steady state of such clouds. It is instead predicted that in the weak embedded convection episode of the APPRAISE clouds, SIP (through the HM process and fragmentation in ice–ice collisions) is the main source for quasi-steady state of ice formation and precipitation. On the other hand, in the long-lived layer-cloud episode of the APPRAISE clouds, the recirculation of dust particles (Fig. 14b and Fig. 15b) is predicted to be the main cause for continuous ice nucleation and precipitation.

In our simulation of summertime deep convection (MC3E) and wintertime orographic clouds (ACAPEX) with some weak embedded convection extending above the  $-36^{\circ}\text{C}$  level, SIP is predicted to initiate about 70%–80% of the total ice at all levels below this level, whereas primary ice only contributes less than 1.5%, implying an IE ratio of about  $10^3$ . In such clouds, the effect of time-dependent ice nucleation on total ice is predicted to be the least. These more convective (MC3E

and less so for ACAPEX) clouds are characterized by typically shorter lifetimes ( $<90$  min) due to stronger vertical motions, suppressing the modest effects from the time dependence of INP activity, relative to the APPRAISE clouds. In the simulated wintertime long-lived ( $\sim 24$  h) stratiform clouds (APPRAISE), the weakness of ascent and shallowness of cloud depth together support less precipitation and hence less SIP, with an IE ratio of only about 10.

To conclude, it is the combination of various SIP mechanisms, interrelated by positive feedbacks of ice multiplication (section 3b), that accurately explains the observed difference between the orders of magnitude of the measured concentrations of INPs and ice particles in the simulated cases. Fragmentation in ice–ice collisions and the HM process are especially pivotal to cloud glaciation. The present study suggests that time-dependent INP activity can be neglected in numerical simulations of clouds, as it has the least impact on the total number of ice particles out of all the ice initiation processes treated. This is consistent with previous laboratory studies (Vali 2014; Ka17; Jk22). Time dependence of INPs cannot explain either the observed ice enhancement in any of the cases of natural clouds studied here or the observed persistence of precipitation of the simulated layer clouds.

*Acknowledgments.* The project was funded mainly through a research grant to Vaughan Phillips (VTJP) from the Swedish Research Council for Sustainable Development (“FORMAS” Award 2018-01795), which supported the first author. This award concerns the effects on clouds and climate arising from the time dependence of ice initiation. VTJP planned and directed the present study. Also, coauthors at Lund were supported by awards to VTJP from the U.S. Department of Energy (DOE) (DE-SC0018932), about ice initiation in clouds, from the Swedish Research Council (“Vetenskapsradet”) about bioaerosol effects on clouds, from the U.S. DOE (DE-SC0018967) with a subaward from the University of Oklahoma

about reasons for high concentrations of ice in clouds, and from Sweden’s Innovation Agency (Vinnova) (2020-03406). The authors thank Jonathan Crosier, Paul Connolly, Ken Carslaw, James Allan, Mian Chin, and Larry Horowitz for their helpful suggestions while setting up the APPRAISE case. The authors also acknowledge Dr. Thomas Bjerring Kristensen for his input while modeling the time-dependent INP freezing in AC. We also would like to thank the editor and three anonymous referees for their insightful comments that helped us to improve the manuscript. The authors declare that there are no competing interests.

*Data availability statement.* The codes representing INP activation (with both time-independent and time-dependent approach) and all four mechanisms of SIP in AC and postprocessing scripts for all three simulated cases are freely available at <https://doi.org/10.5281/zenodo.7654587>. For the simulated MC3E clouds, the observational datasets for microphysical cloud properties are obtained from [https://ghrc.nsstc.nasa.gov/home/field-campaigns/mc3e/data\\_access](https://ghrc.nsstc.nasa.gov/home/field-campaigns/mc3e/data_access) and radar data and the LSF tendencies are obtained from <https://adc.arm.gov/discovery/>. For the simulated ACAPEX case, the microphysical cloud properties dataset is obtained from <ftp://ftp.ucar.edu/pub/mmm/bansemer/acapex/data/>. Also, thermodynamic sounding profile from *Ron Brown* ship is available at <ftp://ftp.ucar.edu/pub/mmm/bansemer/acapex/soundings>. The sounding profiles for the simulation of APPRAISE clouds are taken from the ECMWF ERA5 data over the study domain whereas the observations for cloud microphysical properties are obtained from C11 and W113.

## APPENDIX

### List of Symbols Used in this Paper

Table A1 provides a list of symbols used in the present study along with their units and descriptions.

TABLE A1. Symbols used in the present study along with their units and descriptions.

Symbol	Description	Unit
$A_X$	Proportionality constant for a power law dependence of temperature shift on time	$\text{K s}^{-\beta}$
$D_X$	Diameter of a given aerosol species	$\mu\text{m}$
$H_X$	Fraction reducing INP activity at warm $T$ and low $s_i$ for various groups of aerosols in $X$	—
$n_i$	Number m.r. of ice crystals generated from EP	$\text{kg}^{-1}$
$n_{\text{IN},1,*}$	Background-tropospheric reference activity spectrum number m.r. for water saturation	$\text{kg}^{-1}$
$n_{\text{IN},\text{rain}}$	Number mixing ratio of rain’s activated INP	$\text{kg}^{-1}$
$n_{\text{IN},X}$	Number m.r. of $X$ INP species from the EP	$\text{kg}^{-1}$
$n_X$	Number mixing ratio (m.r.) of APs in group $X$ (not depleted by ice nucleation while inside the cloud)	$\text{kg}^{-1}$
$n_{X,a}$	Number of aerosols in group $X$ lost by ice nucleation	$\text{kg}^{-1}$
$\tilde{n}_{\text{IN},\text{rain}}$	Modified $n_{\text{IN},\text{rain}}$ representing time dependence INP activity	$\text{kg}^{-1}$
$\tilde{n}_{\text{IN},X}$	Modified $n_{\text{IN},X}$ representing time dependence INP activity	$\text{kg}^{-1}$
$Q$	Passive clock tracer	$\text{kg}^{-1}$
$Q_0$	Value of $Q$ outside of the cold cloud (set to unity)	$\text{kg}^{-1}$
$Q_r$	Raindrop’s mass mixing ratio	$\text{kg kg}^{-1}$
$S_i$	Saturation ratio with respect to ice	—
$S_i^w$	Value of $S_i$ at exact water saturation	—
$S_w$	Saturation ratio with respect to water	—

TABLE A1. (Continued)

Symbol	Description	Unit
$t$	Time	s
$t^*$	Time since the start of the isothermal phase of the laboratory experiment (Jk22)	s
$T$	Temperature of ambient air	°C
$w$	Vertical velocity of air	$\text{m s}^{-1}$
$X$	Aerosol species ( $X = \text{DM, BC, sO, FNG, BCT, PLN, and DTS}$ )	—
$z$	Height	m
$\alpha_X$	Fraction of $n_{\text{IN},1,*}$ ( $H_X = 1$ ) from INP activity of AP group $X$	—
$\beta$	Exponent in power-law dependence of temperature shift on time	—
$\gamma_X$	Slope value of the fit for $X$ in FNG, BCT, PLN, DTS	°C <sup>-1</sup>
$\Omega_X$	Total surface area of all APs of diameters larger than $0.1 \mu\text{m}$ from group $X$ (not depleted by ice nucleation while inside the cloud)	(aerosol) $\text{m}^2$ (air) $\text{kg}^{-1}$
$\Omega_{X,1,*}$	Background tropospheric component of $\Omega_X$ for $0.1 \geq D_X \geq 1 \mu\text{m}$	(aerosol) $\text{m}^2$ (air) $\text{kg}^{-1}$
$\Omega_{X,\text{rain}}$	Total surface area of all APs bigger than $0.1 \mu\text{m}$ in group $X$ immersed in liquid raindrops	(aerosol) $\text{m}^2$ (air) $\text{kg}^{-1}$
$\Delta t$	Model time step	s
$\Delta T_X$	Shift in $T$ in time-dependent approach of heterogeneous ice nucleation	K
$\mu_X$	Average number of activated ice embryos per AP in group $X$	—
$\xi(T)$	The function that varies between 0 and 1 for $-5^\circ < T < -2^\circ\text{C}$	—
$\tau_Q$	Relaxation time scale of $\dot{Q}$	s
$v_t$	Fall speeds of raindrops in each size bin	$\text{m s}^{-1}$
$\omega_{X,1,*}$	Baseline coefficient of a group of aerosols from $X = \text{FNG, PLN, BCT, and DTS}$	$\text{m}^2$

## REFERENCES

- Bacon, N. J., B. D. Swanson, M. B. Baker, and E. J. Davis, 1998: Breakup of levitated frost particles. *J. Geophys. Res.*, **103**, 13 763–13 775, <https://doi.org/10.1029/98JD01162>.
- Bigg, E. K., 1953: The supercooling of water. *Proc. Phys. Soc.*, **66B**, 688–694, <https://doi.org/10.1088/0370-1301/66/8/309>.
- Cantrell, W., and A. Heymsfield, 2005: Production of ice in tropospheric clouds: A review. *Bull. Amer. Meteor. Soc.*, **86**, 795–808, <https://doi.org/10.1175/BAMS-86-6-795>.
- Carte, A. E., 1959: Probability of freezing. *Proc. Phys. Soc.*, **73**, 324, <https://doi.org/10.1088/0370-1328/73/2/126>.
- Chen, J.-P., A. Hazra, and Z. Levin, 2008: Parameterizing ice nucleation rates using contact angle and activation energy derived from laboratory data. *Atmos. Chem. Phys.*, **8**, 7431–7449, <https://doi.org/10.5194/acp-8-7431-2008>.
- Clarke, A. D., and Coauthors, 2004: Size distributions and mixtures of dust and black carbon aerosol in Asian outflow: Physiochemistry and optical properties. *J. Geophys. Res.*, **109**, D15S09, <https://doi.org/10.1029/2003JD004378>.
- Connolly, P. J., O. Möhler, P. R. Field, H. Saathoff, R. Burgess, T. Choulaton, and M. Gallagher, 2009: Studies of heterogeneous freezing by three different desert dust samples. *Atmos. Chem. Phys.*, **9**, 2805–2824, <https://doi.org/10.5194/acp-9-2805-2009>.
- Crosier, J., and Coauthors, 2011: Observations of ice multiplication in a weakly convective cell embedded in supercooled mid-level stratus. *Atmos. Chem. Phys.*, **11**, 257–273, <https://doi.org/10.5194/acp-11-257-2011>.
- DeMott, P. J., 1990: An exploratory study of ice nucleation by soot aerosols. *J. Appl. Meteor.*, **29**, 1072–1079, [https://doi.org/10.1175/1520-0450\(1990\)029<1072:AESOIN>2.0.CO;2](https://doi.org/10.1175/1520-0450(1990)029<1072:AESOIN>2.0.CO;2).
- Deshmukh, A., V. T. J. Phillips, A. Bansemmer, S. Patade, and D. Waman, 2022: New empirical formulation for the sublimational breakup of graupel and dendritic snow. *J. Atmos. Sci.*, **79**, 317–336, <https://doi.org/10.1175/JAS-D-20-0275.1>.
- Dong, Y., R. G. Oraltay, and J. Hallett, 1994: Ice particle generation during evaporation. *Atmos. Res.*, **32**, 45–53, [https://doi.org/10.1016/0169-8095\(94\)90050-7](https://doi.org/10.1016/0169-8095(94)90050-7).
- Dudhia, J., 1989: Numerical study of convection observed during the Winter Monsoon Experiment using a mesoscale two-dimensional model. *J. Atmos. Sci.*, **46**, 3077–3107, [https://doi.org/10.1175/1520-0469\(1989\)046<3077:NSOCOD>2.0.CO;2](https://doi.org/10.1175/1520-0469(1989)046<3077:NSOCOD>2.0.CO;2).
- Dufour, L., and R. Defay, 1963: *Thermodynamics of Clouds*. Academic Press, 255 pp.
- Ervens, B., and G. Feingold, 2013: Sensitivities of immersion freezing: Reconciling classical nucleation theory and deterministic expressions. *Geophys. Res. Lett.*, **40**, 3320–3324, <https://doi.org/10.1002/grl.50580>.
- Field, P. R., and A. J. Heymsfield, 2015: Importance of snow to global precipitation. *Geophys. Res. Lett.*, **42**, 9512–9520, <https://doi.org/10.1002/2015GL065497>.
- , —, and A. Bansemmer, 2006: Shattering and particle interarrival times measured by optical array probes in ice clouds. *J. Atmos. Oceanic Technol.*, **23**, 1357–1371, <https://doi.org/10.1175/JTECH1922.1>.
- , and Coauthors, 2017: Secondary ice production: Current state of the science and recommendations for the future. *Ice Formation and Evolution in Clouds and Precipitation: Measurement and Modeling Challenges*, Meteor. Monogr., No. 58, Amer. Meteor. Soc., <https://doi.org/10.1175/AMSMONOGRAPHS-D-16-0014.1>.
- Freidenreich, S. M., and V. Ramaswamy, 1999: A new multiple-band solar radiative parameterization for general circulation models. *J. Geophys. Res.*, **104**, 31 389–31 409, <https://doi.org/10.1029/1999JD900456>.
- Fridlind, A. M., A. S. Ackerman, G. McFarquhar, G. Zhang, M. R. Poellot, P. J. DeMott, A. J. Prenni, and A. J. Heymsfield, 2007: Ice properties of single-layer stratocumulus during the Mixed-Phase Arctic Cloud Experiment: 2. Model results. *J. Geophys. Res.*, **112**, D24202, <https://doi.org/10.1029/2007JD008646>.

- , and Coauthors, 2017: Derivation of aerosol profiles for MC3E convection studies and use in simulations of the 20 May squall line case. *Atmos. Chem. Phys.*, **17**, 5947–5972, <https://doi.org/10.5194/acp-17-5947-2017>.
- Hallett, J., and S. C. Mossop, 1974: Production of secondary ice particles during the riming process. *Nature*, **249**, 26–28, <https://doi.org/10.1038/249026a0>.
- Herbert, R. J., B. J. Murray, T. F. Whale, S. J. Dobbie, and J. D. Atkinson, 2014: Representing time-dependent freezing behaviour in immersion mode ice nucleation. *Atmos. Chem. Phys.*, **14**, 8501–8520, <https://doi.org/10.5194/acp-14-8501-2014>.
- Hobbs, P. V., and J. D. Locatelli, 1969: Ice nuclei from a natural forest fire. *J. Appl. Meteor.*, **8**, 833–834, [https://doi.org/10.1175/1520-0450\(1969\)008<0833:INFANF>2.0.CO;2](https://doi.org/10.1175/1520-0450(1969)008<0833:INFANF>2.0.CO;2).
- , M. K. Politovich, and L. F. Radke, 1980: The structures of summer convective clouds in eastern Montana. I: Natural clouds. *J. Appl. Meteor.*, **19**, 645–663, [https://doi.org/10.1175/1520-0450\(1980\)019<0645:TSOSCC>2.0.CO;2](https://doi.org/10.1175/1520-0450(1980)019<0645:TSOSCC>2.0.CO;2).
- Hong, S.-Y., and H.-L. Pan, 1996: Nonlocal boundary layer vertical diffusion in a medium-range forecast model. *Mon. Wea. Rev.*, **124**, 2322–2339, [https://doi.org/10.1175/1520-0493\(1996\)124<2322:NBLVDI>2.0.CO;2](https://doi.org/10.1175/1520-0493(1996)124<2322:NBLVDI>2.0.CO;2).
- Hoppel, W. A., J. W. Fitzgerald, G. M. Frick, R. E. Larson, and E. J. Mack, 1990: Aerosol size distributions and optical properties found in the marine boundary layer over the Atlantic Ocean. *J. Geophys. Res.*, **95**, 3659–3686, <https://doi.org/10.1029/JD095iD04p03659>.
- Houze, R. A., Jr., 2014. *Cloud Dynamics*. 2nd ed. Elsevier/Academic Press, 496 pp.
- Jakobsson, J. K. F., D. B. Waman, V. T. J. Phillips, and T. Bjerring Kristensen, 2022: Time dependence of heterogeneous ice nucleation by ambient aerosols: Laboratory observations and a formulation for models. *Atmos. Chem. Phys.*, **22**, 6717–6748, <https://doi.org/10.5194/acp-22-6717-2022>.
- James, R. L., V. T. J. Phillips, and P. J. Connolly, 2021: Secondary ice production during the break-up of freezing water drops on impact with ice particles. *Atmos. Chem. Phys.*, **21**, 18 519–18 530, <https://doi.org/10.5194/acp-21-18519-2021>.
- Jennings, S. G., M. Geever, and T. C. O'Connor, 1998: Coastal CCN measurements at Mace Head with enhanced concentrations in strong winds. *Atmos. Res.*, **46**, 243–252, [https://doi.org/10.1016/S0169-8095\(97\)00066-5](https://doi.org/10.1016/S0169-8095(97)00066-5).
- Jensen, M. P., and Coauthors, 2015: The Midlatitude Continental Convective Clouds Experiment (MC3E) sounding network: Operations, processing and analysis. *Atmos. Meas. Tech.*, **8**, 421–434, <https://doi.org/10.5194/amt-8-421-2015>.
- , and Coauthors, 2016: The Midlatitude Continental Convective Clouds Experiment (MC3E). *Bull. Amer. Meteor. Soc.*, **97**, 1667–1686, <https://doi.org/10.1175/BAMS-D-14-00228.1>.
- Kanji, Z. A., L. A. Ladino, H. Wex, Y. Boose, M. Burkert-Kohn, D. J. Cziczko, and M. Krämer, 2017: Overview of ice nucleating particles. *Ice Formation and Evolution in Clouds and Precipitation: Measurement and Modeling Challenges*, *Meteor. Monogr.*, No. 58, Amer. Meteor. Soc., <https://doi.org/10.1175/AMSMONOGRAPHIS-D-16-0006.1>.
- Koop, T., B. Luo, A. Tsias, and T. Peter, 2000: Water activity as the determinant for homogeneous ice nucleation in aqueous solutions. *Nature*, **406**, 611–614, <https://doi.org/10.1038/35020537>.
- Korolev, A. V., E. F. Emery, J. W. Strapp, S. G. Cober, G. A. Isaac, M. Wasey, and D. Marcotte, 2011: Small ice particles in tropospheric clouds: Fact or artifact? Airborne Icing Instrumentation Evaluation experiment. *Bull. Amer. Meteor. Soc.*, **92**, 967–973, <https://doi.org/10.1175/2010BAMS3141.1>.
- Kudzotsa, I., and Coauthors, 2016: Aerosol indirect effects on glaciated clouds. Part I: Model description. *Quart. J. Roy. Meteor. Soc.*, **142**, 1958–1969, <https://doi.org/10.1002/qj.2791>.
- Langham, E. J., and B. J. Mason, 1958: The heterogeneous and homogeneous nucleation of supercooled water. *Proc. Roy. Soc.*, **247A**, 493–504, <https://doi.org/10.1098/rspa.1958.0207>.
- Lasher-Trapp, S., D. C. Leon, P. J. DeMott, C. M. Villanueva-Birriel, A. V. Johnson, D. H. Moser, C. S. Tully, and W. Wu, 2016: A multisensor investigation of rime splintering in tropical maritime cumuli. *J. Atmos. Sci.*, **73**, 2547–2564, <https://doi.org/10.1175/JAS-D-15-0285.1>.
- , E. L. Scott, E. Järvinen, M. Schnaiter, F. Waitz, P. J. DeMott, C. S. McCluskey, and T. C. Hill, 2021: Observations and modeling of rime splintering in Southern Ocean cumuli. *J. Geophys. Res. Atmos.*, **126**, e2021JD035479, <https://doi.org/10.1029/2021JD035479>.
- Lau, K. M., and H. T. Wu, 2003: Warm rain processes over tropical oceans and climate implications. *Geophys. Res. Lett.*, **30**, 2290, <https://doi.org/10.1029/2003GL018567>.
- Lawson, R. P., S. Woods, and H. Morrison, 2015: The microphysics of ice and precipitation development in tropical cumulus clouds. *J. Atmos. Sci.*, **72**, 2429–2445, <https://doi.org/10.1175/JAS-D-14-0274.1>.
- Leung, L. R., 2016: ARM Cloud-Aerosol-Precipitation Experiment (ACAPEX) field campaign report. ARM Rep. DOE/SC-ARM-16-012, 24 pp., <https://www.osti.gov/servlets/purl/1251152>.
- Levin, E. J. T., and Coauthors, 2019: Characteristics of ice nucleating particles in and around California winter storms. *J. Geophys. Res. Atmos.*, **124**, 11 530–11 551, <https://doi.org/10.1029/2019JD030831>.
- Levine, J., 1950: Statistical explanation of spontaneous freezing of water droplets. NACA Tech. 2234, 28 pp., <https://ntrs.nasa.gov/api/citations/19930082877/downloads/19930082877.pdf>.
- Lin, Y., and Coauthors, 2022: Modeling impacts of ice-nucleating particles from marine aerosols on mixed-phase orographic clouds during 2015 ACAPEX field campaign. *Atmos. Chem. Phys.*, **22**, 6749–6771, <https://doi.org/10.5194/acp-22-6749-2022>.
- Lohmann, U., 2006: Aerosol effects on clouds and climate. *Space Sci. Rev.*, **125**, 129–137, <https://doi.org/10.1007/s11214-006-9051-8>.
- Martanda, G., 2022: Fragmentation in graupel-snow collisions. M.S. thesis, Dept. of Physical Geography and Ecosystem Science, Lund University, 47 pp., <http://lup.lub.lu.se/student-papers/record/9087233>.
- Ming, Y., V. Ramaswamy, L. J. Donner, and V. T. J. Phillips, 2006: A new parameterization of cloud droplet activation applicable to general circulation models. *J. Atmos. Sci.*, **63**, 1348–1356, <https://doi.org/10.1175/JAS3686.1>.
- Monin, A. S., and A. M. Obukhov, 1954: Basic laws of turbulent mixing in the atmosphere near the ground. *Tr. Geofiz. Inst., Akad. Nauk SSSR*, **24**, 163–187.
- Mossop, S. C., 1976: Production of secondary ice particles during the growth of graupel by riming. *Quart. J. Roy. Meteor. Soc.*, **102**, 45–57, <https://doi.org/10.1002/qj.49710243104>.
- Murray, B. J., D. O' Sullivan, J. D. Atkinson, and M. E. Webb, 2012: Ice nucleation by particles immersed in supercooled cloud droplets. *Chem. Soc. Rev.*, **41**, 6519–6554, <https://doi.org/10.1039/c2cs35200a>.
- Niedermeier, D., R. A. Shaw, S. Hartmann, H. Wex, T. Clauss, J. Voigtländer, and F. Stratmann, 2011: Heterogeneous ice nucleation: Exploring the transition from stochastic to singular

- freezing behavior. *Atmos. Chem. Phys.*, **11**, 8767–8775, <https://doi.org/10.5194/acp-11-8767-2011>.
- Oraltay, R. G., and J. Hallett, 1989: Evaporation and melting of ice crystals: A laboratory study. *Atmos. Res.*, **24**, 169–189, [https://doi.org/10.1016/0169-8095\(89\)90044-6](https://doi.org/10.1016/0169-8095(89)90044-6).
- Patade, S., and Coauthors, 2021: Empirical formulation for multiple groups of primary biological ice nucleating particles from field observations over Amazonia. *J. Atmos. Sci.*, **78**, 2195–2220, <https://doi.org/10.1175/JAS-D-20-0096.1>.
- , and Coauthors, 2022: The influence of multiple groups of biological ice nucleating particles on microphysical properties of mixed-phase clouds observed during MC3E. *Atmos. Chem. Phys.*, **22**, 12 055–12 075, <https://doi.org/10.5194/acp-22-12055-2022>.
- Pauluis, O., and S. Garner, 2006: Sensitivity of radiative–convective equilibrium simulations to horizontal resolution. *J. Atmos. Sci.*, **63**, 1910–1923, <https://doi.org/10.1175/JAS3705.1>.
- Phillips, V. T. J., L. J. Donner, and S. T. Garner, 2007: Nucleation processes in deep convection simulated by a cloud-system-resolving model with double-moment bulk microphysics. *J. Atmos. Sci.*, **64**, 738–761, <https://doi.org/10.1175/JAS3869.1>.
- , P. J. DeMott, and C. Andronache, 2008: An empirical parameterization of heterogeneous ice nucleation for multiple chemical species of aerosol. *J. Atmos. Sci.*, **65**, 2757–2783, <https://doi.org/10.1175/2007JAS2546.1>.
- , and Coauthors, 2009: Potential impacts from biological aerosols on ensembles of continental clouds simulated numerically. *Biogeosciences*, **6**, 987–1014, <https://doi.org/10.5194/bg-6-987-2009>.
- , P. J. Demott, C. Andronache, K. A. Pratt, K. A. Prather, R. Subramanian, and C. Twohy, 2013: Improvements to an empirical parameterization of heterogeneous ice nucleation and its comparison with observations. *J. Atmos. Sci.*, **70**, 378–409, <https://doi.org/10.1175/JAS-D-12-080.1>.
- , A. Khain, N. Benmoshe, E. Ilotoviz, and A. Ryzhkov, 2015: Theory of time-dependent freezing. Part II: Scheme for freezing raindrops and simulations by a cloud model with spectral bin microphysics. *J. Atmos. Sci.*, **72**, 262–286, <https://doi.org/10.1175/JAS-D-13-0376.1>.
- , J. I. Yano, and A. Khain, 2017a: Ice multiplication by breakup in ice–ice collisions. Part I: Theoretical formulation. *J. Atmos. Sci.*, **74**, 1705–1719, <https://doi.org/10.1175/JAS-D-16-0224.1>.
- , and Coauthors, 2017b: Ice multiplication by breakup in ice–ice collisions. Part II: Numerical simulations. *J. Atmos. Sci.*, **74**, 2789–2811, <https://doi.org/10.1175/JAS-D-16-0223.1>.
- , S. Patade, J. Gutierrez, and A. Bansemmer, 2018: Secondary ice production by fragmentation of freezing drops: Formulation and theory. *J. Atmos. Sci.*, **75**, 3031–3070, <https://doi.org/10.1175/JAS-D-17-0190.1>.
- , and Coauthors, 2020: Multiple environmental influences on the lightning of cold-based continental cumulonimbus clouds. Part I: Description and validation of model. *J. Atmos. Sci.*, **77**, 3999–4024, <https://doi.org/10.1175/JAS-D-19-0200.1>.
- Qu, Z., and Coauthors, 2023: The impacts of secondary ice production on microphysics and dynamics in tropical convection. *EGU sphere*, <https://doi.org/10.5194/egusphere-2022-235>, in press.
- Skamarock, W. C., J. B. Klemp, J. Dudhia, D. O. Gill, D. M. Barker, W. Wang, and J. G. Powers, 2005: A description of the Advanced Research WRF version 2. NCAR Tech. Note NCAR/TN-468+STR, 88 pp., <https://doi.org/10.5065/D6DZ069T>.
- Sotiropoulou, G., S. Sullivan, J. Savre, G. Lloyd, T. Lachlan-Cope, A. M. Ekman, and A. Nenes, 2020: The impact of secondary ice production on Arctic stratocumulus. *Atmos. Chem. Phys.*, **20**, 1301–1316, <https://doi.org/10.5194/acp-20-1301-2020>.
- Takahashi, T., 1978: Riming electrification as a charge generation mechanism in thunderstorms. *J. Atmos. Sci.*, **35**, 1536–1548, [https://doi.org/10.1175/1520-0469\(1978\)035<1536:REAACG>2.0.CO;2](https://doi.org/10.1175/1520-0469(1978)035<1536:REAACG>2.0.CO;2).
- Twomey, S., and T. A. Wojciechowski, 1969: Observations of the geographical variation of cloud nuclei. *J. Atmos. Sci.*, **26**, 648–651, [https://doi.org/10.1175/1520-0469\(1969\)26<648:OOTGVO>2.0.CO;2](https://doi.org/10.1175/1520-0469(1969)26<648:OOTGVO>2.0.CO;2).
- Vali, G., 1994: Freezing rate due to heterogeneous nucleation. *J. Atmos. Sci.*, **51**, 1843–1856, [https://doi.org/10.1175/1520-0469\(1994\)051<1843:FRDTHN>2.0.CO;2](https://doi.org/10.1175/1520-0469(1994)051<1843:FRDTHN>2.0.CO;2).
- , 2008: Repeatability and randomness in heterogeneous freezing nucleation. *Atmos. Chem. Phys.*, **8**, 5017–5031, <https://doi.org/10.5194/acp-8-5017-2008>.
- , 2014: Interpretation of freezing nucleation experiments: Singular and stochastic; sites and surfaces. *Atmos. Chem. Phys.*, **14**, 5271–5294, <https://doi.org/10.5194/acp-14-5271-2014>.
- , and E. J. Stansbury, 1966: Time-dependent characteristics of the heterogeneous nucleation of ice. *Can. J. Phys.*, **44**, 477–502, <https://doi.org/10.1139/p66-044>.
- Vonnegut, B., and M. Baldwin, 1984: Repeated nucleation of a supercooled water sample that contains silver iodide particles. *J. Climate Appl. Meteor.*, **23**, 486–490, [https://doi.org/10.1175/1520-0450\(1984\)023<0486:RNOASW>2.0.CO;2](https://doi.org/10.1175/1520-0450(1984)023<0486:RNOASW>2.0.CO;2).
- Waman, D., S. Patade, A. Jadhav, A. Deshmukh, A. K. Gupta, V. T. J. Phillips, A. Bansemmer, and P. J. DeMott, 2022: Dependencies of four mechanisms of secondary ice production on cloud-top temperature in a continental convective storm. *J. Atmos. Sci.*, **79**, 3375–3404, <https://doi.org/10.1175/JAS-D-21-0278.1>.
- Westbrook, C. D., and A. J. Illingworth, 2013: The formation of ice in a long-lived supercooled layer cloud. *Quart. J. Roy. Meteor. Soc.*, **139**, 2209–2221, <https://doi.org/10.1002/qj.2096>.
- Wright, T. P., and M. D. Petters, 2013: The role of time in heterogeneous freezing nucleation. *J. Geophys. Res. Atmos.*, **118**, 3731–3743, <https://doi.org/10.1002/jgrd.50365>.
- Xie, S., Y. Zhang, S. E. Giangrande, M. P. Jensen, R. McCoy, and M. Zhang, 2014: Interactions between cumulus convection and its environment as revealed by the MC3E sounding array. *J. Geophys. Res. Atmos.*, **119**, 11 784–11 808, <https://doi.org/10.1002/2014JD022011>.
- Yano, J.-I., and V. T. J. Phillips, 2011: Ice–ice collisions: An ice multiplication process in atmospheric clouds. *J. Atmos. Sci.*, **68**, 322–333, <https://doi.org/10.1175/2010JAS3607.1>.
- Yau, M. K., and R. R. Rogers, 1996: *A Short Course in Cloud Physics*. 3rd ed. Elsevier, 304 pp.
- Zhao, X., X. Liu, V. T. Phillips, and S. Patade, 2021: Impacts of secondary ice production on Arctic mixed-phase clouds based on ARM observations and CAM6 single-column model simulations. *Atmos. Chem. Phys.*, **21**, 5685–5703, <https://doi.org/10.5194/acp-21-5685-2021>.